Interrupted Sampling Repeater Jamming Suppression with Pulse Doppler Radar Using Linear Interpulse Frequency Coding

Yueyu GUO [1], Di ZHOU [1,*], Yong DING [2]

[1] Zhejiang Uniview Technologies Co., Ltd, No.369, Xietong Road, Binjiang District, Hangzhou, China
[2] School of Micro-Nano Electronics, Zhejiang University, No.2118, Pinglan Road, Xiaoshan District, Hangzhou, China

guoyueyu202105@126.com, zhoudi@uniview.com*, dingyong09@zju.edu.cn

Abstract. *Interrupted sampling repeater jamming (ISRJ) is an advanced form of coherent jamming, and the suppression of this jamming has become a critical problem for modern radar electronic countermeasures. In this paper, we propose a countermeasure based on the linear interpulse frequency-coding linear frequency modulation (LIFC-LFM) signal. The LIFC refers to the linear encoding of the frequency of each pulse transmitted by the radar system, which can change the distribution of the false targets formed by ISRJ in the range-Doppler (RD) spectrum. In this context, we design the frequency coding value to effectively separate the true and false targets in the RD spectrum. Furthermore, we propose a fast-time phase compensation method to separate the true and false targets in the Doppler dimension to facilitate false target suppression. Finally, ISRJ can be suppressed by oblique projection processing. Simulation examples demonstrate that the proposed method has an excellent and robust ISRJ suppression effect for direct forwarding ISRJ, repeated forwarding ISRJ, and frequency shifting ISRJ. Meanwhile, the signal-to-noise ratio loss caused by the jamming suppression is small.*

Keywords

Pulse-Doppler radar, deception jamming suppression, interrupted sampling repeater jamming, interpulse frequency coding, oblique projection processing, ambiguity function

1. Introduction

Modern complex battlefield electromagnetic environments require radar systems with reliable jamming countermeasures. With the development of digital radiofrequency memory (DRFM) technology [1], [2], deception jamming has been widely used in electronic warfare to deceive radar systems. Among the various deception jamming methods, interrupted sampling repeater jamming (ISRJ) [3], [4] is one of the most difficult to counter. Jamming is generated by a jammer using DRFM technology to rapidly sample and forward radar signals. It has the following advantages: (i) ISRJ is a type of intra-pulse jamming and has a fast response speed [5]; (ii) ISRJ can form multiple false targets after pulse compression, which has both suppression and deception effects [3]; and (iii) the jamming modulation mode is flexible, and the jammer can generate different types of ISRJ with different effects based on different forwarding and modulation methods, such as direct forwarding ISRJ, repeated forwarding ISRJ, and frequency shifting ISRJ [5].

Compared to repeater jamming delayed by more than one pulse repetition interval [6–14], research on the ECCM methods of the ISRJ is relatively scarce. In open literature studies, ISRJ countermeasures can be divided into two main types: ISRJ suppression methods based on signal processing [15–19] and ISRJ suppression methods based on waveform design [20–24].

In terms of signal processing, filtering and cancellation methods for ISRJ suppression have been proposed [15–19]. In [15], a band-pass filter was designed to filter out the ISRJ using the discontinuity characteristics of the ISRJ in the time-frequency domain. The jamming parameters used for the bandpass filter design were estimated using time-frequency (TF) analysis. Since the method proposed in [15] only considers point targets, an efficient filtering method for wideband radars has been proposed [16]. Moreover, a filtering method based on energy function detection was proposed in [17], which is not necessary for performing complicated time-frequency analyses. Considering that [17] has poor extraction of jamming-free signal segments under the condition of low signal to interference plus noise power ratio (SINR), a modified method based on max-TF function detection was proposed in [18]. In addition to filtering methods, a reconstruction and cancellation method for ISRJ suppression has been proposed in [19]. The parameters used for jamming reconstruction were estimated using TF analysis and deconvolution processing.

In addition to signal processing, waveform design is also an effective method for solving jamming problems. The waveform design method is more effective in anti-jamming than the signal-processing method. Exploiting the fact that the jammer can only intercept some of the radar signal frag-

ments, an in-pulse quadrature phase-frequency encoding waveform is designed to mismatch the ISRJ with radar signal fragments that are not intercepted [20]. Using this ISRJ countermeasure mechanism, the work of adopting the immune algorithm and improved genetic algorithm to design the quadrature-phase encoding waveform has been proposed successively [21], [22]. However, the antijamming performance of the methods presented in [20–22] is related to the orthogonality of the designed waveforms. To further improve the radar anti-jamming performance, a joint design method for the transmit waveform and mismatch filter was proposed [23–26]. Furthermore, a countermeasure based on the waveform agility was proposed to solve the target echo cancellation problem caused by the frequency-shifting ISRJ [5].

The above methods can effectively suppress the ISRJ under appropriate conditions; however, some problems remain. First, these methods cannot achieve effective separation of the target echo signal and ISRJ; therefore, the jamming-suppression performance is limited. Second, they are mostly proposed for a certain type of ISRJ and cannot suppress multiple types of ISRJ. In this paper, we present a novel ISRJ countermeasure based on a linear interpulse frequency-coding linear frequency modulation (LIFC-LFM) signal. By designing the LIFC-LFM signal, the target echo signal and ISRJ can be effectively separated in the range-Doppler (RD) spectrum. Furthermore, an ISRJ suppression method based on Doppler filtering is proposed. The contributions of this study are summarized as follows:

(1) An LIFC-LFM signal design for ISRJ separation is proposed. LIFC refers to the linear encoding of the frequency of each pulse transmitted by a radar system. This can cause false targets formed by the ISRJ to be distributed obliquely in the RD spectrum, thus realizing separation from the true target. The separation performance can be controlled using an inter-pulse frequency coding value design. Compared to existing methods, this method fully exploits the advantages of waveform design in active anti-jamming. It can separate true and false targets in the RD spectrum. In addition, the design of the interpulse frequency coding value does not require complex optimization, which fulfils the real-time demands of the battlefield. Additionally, this method works for direct forwarding ISRJ, repeated forwarding ISRJ, and frequency-shifting ISRJ.

(2) An LIFC-LFM signal processing method is proposed for ISRJ suppression. The false targets formed by the ISRJ are obliquely distributed in the RD spectrum and are difficult to suppress. Therefore, we propose a RD rotation transformation method based on fast time-phase compensation, shifting the false targets to the same Doppler frequency unit. Furthermore, oblique projection processing [27–29] is used to suppress jamming. Since the target echo signal and ISRJ are separated when filtering out the ISRJ, the proposed method can achieve an excellent ISRJ suppression effect with a low signal-to-noise ratio (SNR) loss.

2. LIFC-LFM Signal Modelling and Analysis

2.1 LIFC-LFM Signal

Linear interpulse frequency coding linear frequency modulation (LIFC-LFM) signal refers to the linear frequency modulation (LFM) pulse train signal encoded by linear frequency between pulses, which can be represented as follows:

$$s(t) = \sum_{n=0}^{N-1} u(t - nT_r)\exp(j2\pi f_n t) = \sum_{n=0}^{N-1} u(t - nT_r)\exp(j2\pi n\Delta f t) \quad (1)$$

where N indicates the number of pulses in a coherent process interval (CPI). T_r indicates the pulse repetition interval (PRI). $f_n = n\Delta f$ is the frequency coding of the $(n + 1)$-th pulse, where Δf denotes the unit frequency step. $u(t)$ represents the complex envelope of the LFM signal with pulse width T, which is expressed as follows:

$$u(t) = \text{rect}\left(\frac{t}{T}\right)\exp(j\pi k t^2) \quad (2)$$

where $k = B/T$ is the frequency slope, and B denotes the bandwidth of $u(t)$. Additionally, $\text{rect}(t)$ is the rectangular function,

$$\text{rect}(t) = \begin{cases} 1, & 0 \le t < 1 \\ 0, & \text{else} \end{cases}. \quad (3)$$

The frequency encoding scheme of the LIFC-LFM signal is the same as that of the stepped frequency (SF) signal [30], [31]; however, the purpose of frequency encoding and the magnitude of the frequency coding values are different. The unit frequency step Δf of the SF pulse signal is generally set to a larger value to achieve large overall bandwidth. In contrast, the absolute value of Δf in (1) is set to a small value, satisfying $|\Delta f| \ll B$, which may cause the false targets formed by ISRJ to be obliquely distributed obliquely in the RD spectrum.

2.2 Ambiguity Function Analysis

The ambiguity function (AF) [32], [33] is one of the most commonly used and important signal analysis tools for visually demonstrating echo distribution characteristics. Since the LIFC-LFM signal has the same form as the SF pulse signal, their AF expressions are also the same. The AF expression of the LIFC-LFM signal is as follows:

$$\chi(\tau, f_d) = \int_{-\infty}^{+\infty} s(t + \tau)s^*(t)\exp(j2\pi f_d t)\,dt \quad (4)$$

where τ indicates the delay in the target echo. In this study, we consider the center AF of the LIFC-LFM signal, that is, $|\tau| < T$, $|f_d| < 1/(2T_r)$. Therefore, we apply (1) to (4) and obtain

$$\chi(\tau, f_{\mathrm{d}}) = \sum_{n=0}^{N-1} \int_{-\infty}^{+\infty} \begin{bmatrix} u(t+\tau-nT_{\mathrm{r}})\exp(\mathrm{j}2\pi f_{n}(t+\tau)) \\ u^{*}(t-nT_{\mathrm{r}})\exp(-\mathrm{j}2\pi f_{n}t) \end{bmatrix} \exp(\mathrm{j}2\pi f_{\mathrm{d}}t)\mathrm{d}t \overset{t'=t-nT_{r}}{=}$$

$$\sum_{n=0}^{N-1}\exp(\mathrm{j}2\pi f_{n}\tau + \mathrm{j}2\pi f_{\mathrm{d}}nT_{\mathrm{r}})\int_{-\infty}^{+\infty}u(t'+\tau)u^{*}(t')\exp(\mathrm{j}2\pi f_{\mathrm{d}}t')\mathrm{d}t' =$$

$$\left[\sum_{n=0}^{N-1}\exp(\mathrm{j}2\pi n(f_{\mathrm{d}}T_{\mathrm{r}}+\Delta f\tau))\right]\left[\int_{-\infty}^{+\infty}u(t+\tau)u^{*}(t)\exp(\mathrm{j}2\pi f_{\mathrm{d}}t)\mathrm{d}t\right] =$$

$$\exp(\mathrm{j}\pi(f_{\mathrm{d}}T_{\mathrm{r}}+\Delta f\tau)(N-1))\frac{\sin(N\pi(f_{\mathrm{d}}T_{\mathrm{r}}+\Delta f\tau))}{\sin(\pi(f_{\mathrm{d}}T_{\mathrm{r}}+\Delta f\tau))}\chi_{\mathrm{LFM}}(\tau, f_{\mathrm{d}})$$

(5)

where $\chi_{\mathrm{LFM}}(\tau, f_{\mathrm{d}})$ represents the AF of LFM signal $u(t)$,

$$\chi_{\mathrm{LFM}}(\tau, f_{\mathrm{d}}) = \int_{-\infty}^{+\infty}u(t+\tau)u^{*}(t)\exp(\mathrm{j}2\pi f_{\mathrm{d}}t)\mathrm{d}t =$$

$$\exp(\mathrm{j}\pi k\tau^{2})\exp(\mathrm{j}\pi(k\tau+f_{\mathrm{d}})(T-\tau))$$

(6)

$$\frac{\sin(\pi(k\tau+f_{\mathrm{d}})(T-|\tau|))}{\pi(k\tau+f_{\mathrm{d}})}.$$

The Doppler mainlobe width of $\chi_{\mathrm{LFM}}(\tau, f_{\mathrm{d}})$ is approximately equal to $1/T$. Since $|f_{\mathrm{d}}|<1/(2T_{\mathrm{r}})<1/T$, $\chi_{\mathrm{LFM}}(\tau, f_{\mathrm{d}}) \approx \chi_{\mathrm{LFM}}(\tau, 0)$. Therefore, equation (5) can be rewritten as

$$\chi(\tau, f_{\mathrm{d}}) \approx \exp(\mathrm{j}\pi(f_{\mathrm{d}}T_{\mathrm{r}}+\Delta f\tau)(N-1))$$

$$\frac{\sin(N\pi(f_{\mathrm{d}}T_{\mathrm{r}}+\Delta f\tau))}{\sin(\pi(f_{\mathrm{d}}T_{\mathrm{r}}+\Delta f\tau))}\chi_{\mathrm{LFM}}(\tau, 0)=$$

$$\exp(\mathrm{j}\pi(f_{\mathrm{d}}T_{\mathrm{r}}+\Delta f\tau)(N-1)+\mathrm{j}\pi kT\tau)$$

(7)

$$\frac{\sin(N\pi(f_{\mathrm{d}}T_{\mathrm{r}}+\Delta f\tau))}{\sin(\pi(f_{\mathrm{d}}T_{\mathrm{r}}+\Delta f\tau))}\frac{\sin(\pi k\tau(T-|\tau|))}{\pi k\tau}.$$

According to (7), the peak position of the ambiguity function satisfies $f_{\mathrm{d}}T_{\mathrm{r}} + \Delta f\tau = 0$ and $\tau = 0$, which means the mainlobe of the ambiguity function is located at the origin. Additionally, the AF of the LIFC-LFM signal was obliquely distributed by the slope $k_{\Delta f}$:

$$k_{\Delta f} = \frac{f_{\mathrm{d}}}{\tau} = -\frac{\Delta f}{T_{\mathrm{r}}}.$$

(8)

It shows that the AF of the LIFC-LFM signal has a RD coupling effect, which leads to the broadening of its Doppler mainlobe. The delay mainlobe width of the LFM pulse train signal is approximately $1/B$, and its Doppler mainlobe width is approximately $1/NT_{\mathrm{r}}$. Under the same parameters, the delay mainlobe width of the LIFC-LFM signal is approximately $1/B$, but its Doppler mainlobe width is different from that of the LFM pulse train signal. The Doppler mainlobe width is approximately equal to that of the $|k_{\Delta f}|/B + 1/(NT_{\mathrm{r}})$. For ease of understanding, Figure 1 presents a comparison of the AF mainlobe of the LFM pulse train signal and LIFC-LFM signal.

To alleviate the Doppler resolution degradation caused by Doppler broadening, we can design the unit frequency step
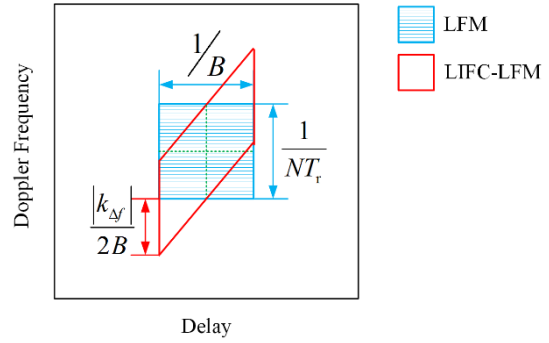

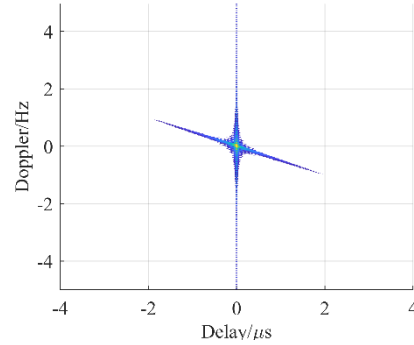Fig. 1.   Schematic of the AF mainlobe.

Fig. 2.   Ambiguity function of the LIFC-LFM signal.

Δf such that the Doppler broadening is less than $1/(NT_{\mathrm{r}})$, which satisfies the following equation

$$\frac{|k_{\Delta f}|}{B} < \frac{1}{NT_{\mathrm{r}}}.$$

(9)

Substituting (8) into (9) yields

$$|\Delta f| < \frac{B}{N}.$$

(10)

It can be observed that the LIFC-LFM signal has a "thumbtack" AF if we ignore the sidelobe of the ambiguity function $\chi(\tau, f_{\mathrm{d}})$ and assign a smaller value to $|\Delta f|$. Figure 2 shows the AF simulation results for the LIFC-LFM signal. In the simulation, the radar signal has the following parameters: $T_{\mathrm{r}} = 100$ μs, $T = 10$ μs, $B = 50$ MHz, $N = 128$, and $\Delta f = 50$ kHz.

2.3 LIFC-LFM Signal Echo Analysis

Suppose that there exists a threat target in the far field. The delay and Doppler frequency of the target are τ_{s} and $f_{\mathrm{d,s}}$, respectively, where $T < \tau_{\mathrm{s}} < T_{\mathrm{r}} - T$ and $|f_{\mathrm{d,s}}| < 1/(2T_{\mathrm{r}})$. The target echo received by the radar in the $(n+1)$-th PRI is denoted as $x_{\mathrm{s},n}(t)$:

$$x_{\mathrm{s},n}(t) = A_{\mathrm{s}}u(t-nT_{\mathrm{r}}-\tau_{\mathrm{s}})$$

$$\exp(\mathrm{j}2\pi f_{n}(t-\tau_{\mathrm{s}}))\exp(\mathrm{j}2\pi f_{\mathrm{d,s}}t)$$

(11)

where A_{s} denotes the complex amplitude. We performed matching processing on the echo, and the reference signal in the $(n+1)$-th PRI is $[u(t-nT_{\mathrm{r}})\exp(\mathrm{j}2\pi f_{n}t)]^{*}$. The matching process result can then be expressed as follows:

$$r_{s,n}(t) = x_{s,n}(t) \otimes \left[u(-t - nT_r)\exp\left(j2\pi f_n(-t)\right)\right]^* =$$

$$\int_{-\infty}^{+\infty} x_{s,n}(t-\tau)\left[u(-\tau - nT_r)\exp\left(j2\pi f_n(-\tau)\right)\right]^* d\tau =$$

$$\int_{-\infty}^{+\infty} \begin{bmatrix} A_s u(t-\tau_s-\tau-nT_r) \\ \exp\left(j2\pi f_n(t-\tau_s-\tau)+j2\pi f_{d,s}(t-\tau)\right) \end{bmatrix}^{\tau'=-\tau-nT_r} \\ \left[u^*(-\tau-nT_r)\exp\left(j2\pi f_n\tau\right)\right] d\tau \quad (12)$$

$$\int_{-\infty}^{+\infty} \begin{bmatrix} A_s u(\tau'+t-\tau_s) \\ \exp\left(j2\pi f_n(t-\tau_s)+j2\pi f_{d,s}(t+\tau'+nT_r)\right) \end{bmatrix} u^*(\tau') d\tau' =$$

$$A_s \exp\left(j2\pi f_n(t-\tau_s)\right)\exp\left(j2\pi f_{d,s}(t+nT_r)\right)$$

$$\int_{-\infty}^{+\infty} u(\tau+t-\tau_s)u^*(\tau)\exp\left(j2\pi f_{d,s}\tau\right) d\tau.$$

As we consider only $|f_{d,s}| < 1/(2T_r) < 1/T$, equation (12) can be rewritten as follows:

$$r_{s,n}(t) \approx A_s \exp\left(j2\pi f_n(t-\tau_s)\right)$$

$$\exp\left(j2\pi f_{d,s}(t+nT_r)\right)\int_{-\infty}^{+\infty} u(\tau+t-\tau_s)u^*(\tau) d\tau. \quad (13)$$

Furthermore, we performed Doppler coherent processing on the target echo received in N PRIs, and the Doppler compensation value is denoted as f_d. The processing result is

$$r_s(t,f_d) = \sum_{n=0}^{N-1} r_{s,n}(t)\exp\left(-j2\pi f_d nT_r\right) \approx$$

$$A_s \sum_{n=0}^{N-1}\exp\left(j2\pi f_n(t-\tau_s)\right)\exp\left(j2\pi f_{d,s}(t+nT_r)\right)\exp\left(-j2\pi f_d nT_r\right)$$

$$\int_{-\infty}^{+\infty} u(\tau+t-\tau_s)u^*(\tau) d\tau \quad (14)$$

$$= A_s\exp\left(j2\pi f_{d,s}t\right)\left[\sum_{n=0}^{N-1}\exp\left\{j2\pi\left[\Delta f(t-\tau_s)+\left(f_{d,s}-f_d\right)T_r\right]n\right\}\right]$$

$$\left[\int_{-\infty}^{+\infty} u(\tau+t-\tau_s)u^*(\tau) d\tau\right].$$

According to (5) and (7),

$$\chi(\tau,f_d) \approx \left[\sum_{n=0}^{N-1}\exp\left(j2\pi n\left(f_d T_r+\Delta f\tau\right)\right)\right]\left[\int_{-\infty}^{+\infty} u(t+\tau)u^*(t) dt\right]. \quad (15)$$

Therefore, equation (15) can be rewritten as

$$r_s(t,f_d) \approx A_s\exp\left(j2\pi f_{d,s}t\right)\chi\left(t-\tau_s,-\left(f_d-f_{d,s}\right)\right). \quad (16)$$

It can be observed that the target echo forms a peak at $(R_s, f_{d,s})$ after RD processing, where $R_s = c\tau_s/2$ and c denotes the speed of light. Therefore, the target can be accurately detected by transmitting the LIFC-LFM signal.
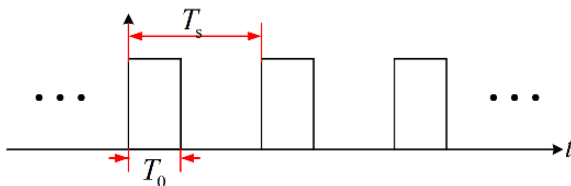

Fig. 3. Illustration of interrupted sampling function.

3. Interrupted Sampling Repeater Jamming Analysis

3.1 Principle of Interrupted Sampling Repeater Jamming

The ISRJ is formed by jammer sampling and the forwarding of radar signals. In practice, the jammer begins sampling when a radar pulse front is detected, stops sampling at the end of the pulse, and restarts sampling when the next pulse front is detected. This process is repeated. The interrupted sampling function $p(t)$ adopted by the jammer is a rectangular envelope pulse train

$$p(t) = \text{rect}\left(\frac{t}{T_0}\right) \otimes \sum_{l=-\infty}^{+\infty}\delta(t-lT_s) \quad (17)$$

where T_0 represents the sampling pulse duration, l is an integer, and T_s denotes the sampling period. Figure 3 shows a diagram of the interrupted sampling function.

Therefore, the sampled signal $s_{\text{sample}}(t)$ obtained by jammer sampling of the LIFC-LFM signal can be expressed as

$$s_{\text{sample}}(t) = \sum_{n=0}^{N-1} p(t-nT_r)u(t-nT_r)\exp\left(j2\pi f_n t\right) = \sum_{n=0}^{N-1} s_{\text{sample},n}(t) \quad (18)$$

where

$$s_{\text{sample},n}(t) = p(t-nT_r)u(t-nT_r)\exp\left(j2\pi f_n t\right). \quad (19)$$

Furthermore, the jammer repeatedly transmits the sampled signal $s_{\text{sample}}(t)$ with frequency shift f_J to interfere with the radar. The ISRJ signal $s_J(t)$ can be expressed as

$$s_J(t) = \sum_{m=0}^{M-1}\sum_{n=0}^{N-1} s_{\text{sample},n}(t-mT_0)\exp\left(j2\pi f_J(t-mT_0-nT_r)\right) = \sum_{n=0}^{N-1} s_{J,n}(t) \quad (20)$$

where M indicates the number of forwardings, and $s_{J,n}(t)$ is the ISRJ signal generated in the $(n+1)$-th PRI.

$$s_{J,n}(t) = \sum_{m=0}^{M-1} s_{\text{sample},n}(t-mT_0)\exp\left(j2\pi f_J(t-mT_0-nT_r)\right) =$$

$$\sum_{m=0}^{M-1} p(t-nT_r-mT_0)u(t-nT_r-mT_0)\exp\left(j2\pi f_n(t-mT_0)\right)\exp\left(j2\pi f_J(t-mT_0-nT_r)\right). \quad (21)$$

According to [34], $p(t)u(t)$ is equivalently expressed as

$$p(t)u(t) = \sum_{l=-\infty}^{+\infty} a_l u(t)\exp\left(j2\pi l f_s t\right) \quad (22)$$

where

$$a_l = \exp\left(-j\pi T_0 l f_s\right)T_0 f_s\,\text{sa}\left(\pi T_0 l f_s\right) \quad (23)$$

where $f_s = 1/T_s$ and $\text{sa}(x) = \sin(x)/x$. Therefore, equation (21) can be rewritten as follows:

$$s_{J,n}(t) = \sum_{m=0}^{M-1}\sum_{l=-\infty}^{+\infty}\begin{matrix} a_l u(t-nT_r-mT_0) \\ \exp\begin{pmatrix} j2\pi l f_s(t-nT_r-mT_0)+ \\ j2\pi f_n(t-mT_0)+j2\pi f_J(t-mT_0-nT_r) \end{pmatrix} \end{matrix}. \quad (24)$$
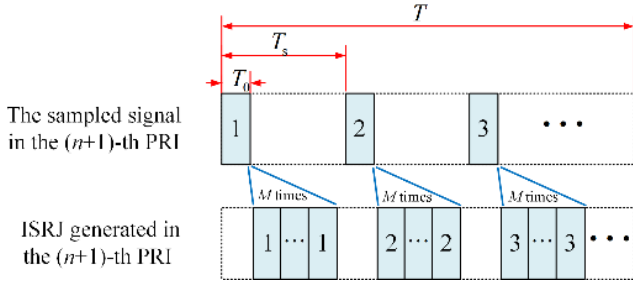
Fig. 4. Diagram of the ISRJ generated in the $(n+1)$-th PRI.

Based on the different values of M and f_J, $s_J(t)$ represents the different ISRJs. First, when $M = 0$ and $f_J = 0$, $s_J(t)$ directly forwards the ISRJ. Second, when $M \neq 0$ and $f_J = 0$, $s_J(t)$ represents repeated forwarding ISRJ. Third, when $f_J \neq 0$, $s_J(t)$ denotes frequency shifting ISRJ. Figure 4 shows

the ISRJ forwarded by the jammer in the $(n+1)$-th PRI, where the forwarding number is M.

3.2 Cross Ambiguity Function Analysis

In this subsection, we adopt the cross-ambiguity function (CAF) [35] to analyze the ISRJ, which can visually demonstrate the ISRJ distribution characteristics after RD processing. The CAF of the LIFC-LFM signal and ISRJ are

$$\psi(\tau, f_d) = \int_{-\infty}^{+\infty} s_J(t + \tau) s^*(t) \exp(j2\pi f_d t) dt . \qquad (25)$$

In this paper, we only consider the center CAF, that is, $|\tau| < T$, $|f_d| < 1/2T_r$. Substituting (1), (20), and (21) into (25) yields (26)

$$\psi(\tau, f_d) = \sum_{n=0}^{N-1} \int_{-\infty}^{+\infty} \left\{ \begin{array}{l} \left[\sum_{m=0}^{M-1} \sum_{l=-\infty}^{+\infty} a_l u(t + \tau - nT_r - mT_0) \exp\left(j2\pi l f_s(t + \tau - nT_r - mT_0) + j2\pi f_n(t + \tau - mT_0) \right) \right. \\ \left. \cdot \exp\left(j2\pi f_J(t - mT_0 + \tau - nT_r) \right) \right] \left[u(t - nT_r) e^{j2\pi f_n t} \right]^* e^{j2\pi f_d t} \end{array} \right\} \Bigg|_{t'=t-nT_r} dt =$$

$$\sum_{m=0}^{M-1} \sum_{l=-\infty}^{+\infty} a_l \exp\left(j2\pi (lf_s + f_J)(\tau - mT_0) \right) \left\{ \sum_{n=0}^{N-1} \exp\left\{ j2\pi \left[\Delta f(\tau - mT_0) + f_d T_r \right] n \right\} \right\}$$

$$\int_{-\infty}^{+\infty} u(t' + \tau - mT_0) u^*(t') \exp\left(j2\pi (lf_s + f_J + f_d) t' \right) dt' = \qquad (26)$$

$$\sum_{m=0}^{M-1} \sum_{l=-\infty}^{+\infty} a_{m,l}(\tau, f_d) \frac{\sin\left(\pi \left[\Delta f(\tau - mT_0) + f_d T_r \right] N \right)}{\sin\left(\pi \left[\Delta f(\tau - mT_0) + f_d T_r \right] \right)} \chi_{\text{LFM}}(\tau - mT_0, lf_s + f_J + f_d) =$$

$$\sum_{m=0}^{M-1} \psi_m(\tau, f_d)$$

where $a_{m,l}(\tau, f_d)$ is a complex coefficient,

$$a_{m,l}(\tau, f_d) = a_l \exp\left\{ \begin{array}{l} j2\pi (lf_s + f_J)(\tau - mT_0) + \\ j\pi \left[\Delta f(\tau - mT_0) + f_d T_r \right](N-1) \end{array} \right\} \qquad (27)$$

and $\psi_m(\tau, f_d)$ is the CAF of the LIFC-LFM signal and jamming signal forwarded by the jammer for the $(m+1)$-th time. The CAF $\psi(\tau, f_d)$ comprises multiple $\psi_m(\tau, f_d)$ with different time shifts:

$$\psi_m(\tau, f_d) = \sum_{l=-\infty}^{+\infty} a_{m,l}(\tau, f_d) \frac{\sin\left(\pi \left[\Delta f(\tau - mT_0) + f_d T_r \right] N \right)}{\sin\left(\pi \left[\Delta f(\tau - mT_0) + f_d T_r \right] \right)} . \qquad (28)$$
$$\chi_{\text{LFM}}(\tau - mT_0, lf_s + f_J + f_d)$$

Since we only consider $|f_d| < 1/(2T_r) < 1/T$, $\chi_{\text{LFM}}(\tau - mT_0, lf_s + f_J + f_d) \approx \chi_{\text{LFM}}(\tau - mT_0, lf_s + f_J)$. Therefore, equation (28) can be rewritten as

$$\psi_m(\tau, f_d) \approx \sum_{l=-\infty}^{+\infty} a_{m,l}(\tau, f_d) \frac{\sin\left(\pi \left[\Delta f(\tau - mT_0) + f_d T_r \right] N \right)}{\sin\left(\pi \left[\Delta f(\tau - mT_0) + f_d T_r \right] \right)} . \qquad (29)$$
$$\chi_{\text{LFM}}(\tau - mT_0, lf_s + f_J)$$

In (29), the first term on the right-hand side of the equation is a complex amplitude term that can be ignored. The second term is the sinc function, which has a peak output when the condition $\Delta f(\tau - mT_0) + f_d T_r = 0$ is satisfied. The third term is the delay cut of the ambiguity function

$\chi_{\text{LFM}}(\tau - mT_0, f_d)$ at the Doppler frequency shift point $(lf_s + f_J)$, which has a peak output when the condition $k(\tau - mT_0) + (lf_s + f_J) = 0$ is satisfied. Therefore, the CAF $\psi_m(\tau, f_d)$ has multiple peak outputs, and the peak output numbered l is located at $(mT_0 - (lf_s + f_J)/k, \Delta f(lf_s + f_J)/kT_r)$. Since

$$\frac{\Delta f(lf_s + f_J)/kT_r - 0}{\left(mT_0 - lf_s + f_J/k \right) - mT_0} = -\frac{\Delta f}{T_r} = k_{\Delta f} \qquad (30)$$

it is evident that the peak outputs of the CAF $\psi_m(\tau, f_d)$ are distributed on the oblique line passing through point $(mT_0, 0)$, and the slope of the oblique line is $k_{\Delta f}$. It is noteworthy that the pulse train signal is periodic in the Doppler dimension. When the slope $k_{\Delta f}$ is large, the peak outputs of the CAF $\psi_m(\tau, f_d)$ may appear periodically in the cross-ambiguity function diagram. Figure 5 shows the CAF simulation results of the LFM pulse train signal and the RIFC-LFM signal. In the simulation, $T_0 = 0.5$ μs, $T_s = 2$ μs, $M = 3$, $f_J = 0$ Hz, and other parameters are the same as mentioned above.

3.3 Interrupted Sampling Repeater Jamming Echo Analysis

Suppose that there is a threat target in the far field. The delay and Doppler frequency of the target are τ_s and $f_{d,s}$, respectively, where $T < \tau_s < T_r - T$ and $|f_{d,s}| < 1/(2T_r)$. The target

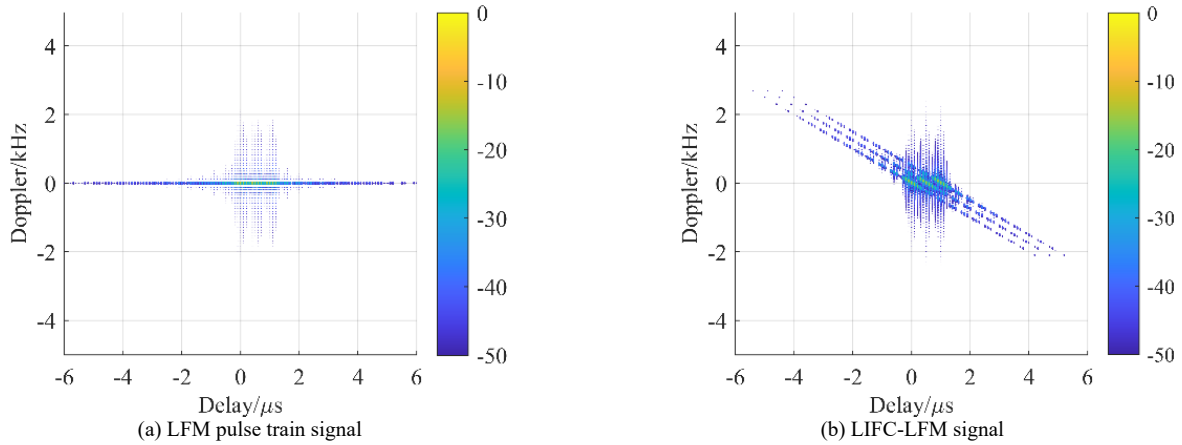(a) LFM pulse train signal (b) LIFC-LFM signal

Fig. 5. Cross ambiguity function top view.

is equipped with a self-defense jammer that could generate an ISRJ. The ISRJ signal received by the radar in the $(n+1)$ PRI is denoted by $x_{J,n}(t)$:

$$
\begin{aligned}
x_{J,n}(t) &= A_J s_{J,n}(t - \tau_J)\exp(j2\pi f_{d,s}t) = \\
&A_J \sum_{m=0}^{M-1}\sum_{l=-\infty}^{+\infty} a_l u(t - nT_r - mT_0 - \tau_J) \\
&\exp(j2\pi l f_s(t - nT_r - mT_0 - \tau_J)) \\
&\cdot\exp\!\begin{pmatrix} j2\pi f_n(t - mT_0 - \tau_J) + \\ j2\pi f_J(t - mT_0 - nT_r - \tau_J) + j2\pi f_{d,s}t \end{pmatrix}
\end{aligned}
\tag{31}
$$

where A_J indicates the amplitude of the ISRJ signal. Furthermore, τ_J indicates the delay of the ISRJ signal, which satisfies $\tau_s < \tau_J < T_r$ and $\tau_J - \tau_s > T_0$. We performed matching processing on the ISRJ signal, and the reference signal in the $(n+1)$ PRI is $[u(t - nT_r)\exp(j2\pi f_n t)]^*$. The matching process result can then be expressed as follows in (32).

Furthermore, we performed Doppler coherent processing on the echo received in N PRIs, and the Doppler compensation value is denoted as f_d. The processing result is given in (33).

$$
\begin{aligned}
r_{J,n}(t) &= x_{J,n}(t) \otimes \left[u(-t - nT_r)\exp(j2\pi f_n(-t))\right]^* = \int_{-\infty}^{+\infty} x_{J,n}(t - \tau)\left[u(-\tau - nT_r)\exp(j2\pi f_n(-\tau))\right]^* d\tau = \\
&\int_{-\infty}^{+\infty}\left\{\begin{array}{l}\left[A_J\sum_{m=0}^{M-1}\sum_{l=-\infty}^{+\infty} a_l u(t - \tau - nT_r - mT_0 - \tau_J)\exp(j2\pi l f_s(t - \tau - nT_r - mT_0 - \tau_J) + j2\pi f_n(t - \tau - mT_0 - \tau_J))\right. \\ \left.\exp(j2\pi f_J(t - \tau - mT_0 - nT_r - \tau_J) + j2\pi f_{d,s}(t - \tau))\right]\cdot\left[u^*(-\tau - nT_r)\exp(j2\pi f_n\tau)\right]\end{array}\right\}d\tau \overset{\tau'=-\tau-nT_r}{=} \\
&\int_{-\infty}^{+\infty}\left\{\begin{array}{l}\left[A_J\sum_{m=0}^{M-1}\sum_{l=-\infty}^{+\infty} a_l u(t + \tau' - mT_0 - \tau_J)\exp(j2\pi l f_s(t + \tau' - mT_0 - \tau_J) + j2\pi f_n(t - mT_0 - \tau_J))\right. \\ \left.\exp(j2\pi f_J(t + \tau' - mT_0 - \tau_J) + j2\pi f_{d,s}(t + \tau' + nT_r))\right]\cdot u^*(\tau')\end{array}\right\}d\tau' = \\
&A_J\sum_{m=0}^{M-1}\sum_{l=-\infty}^{+\infty} a_l \exp\left(j2\pi(l f_s + f_J)(t - mT_0 - \tau_J) + j2\pi f_{d,s}t\right)\exp\left\{j2\pi\left[\Delta f(t - mT_0 - \tau_J) + f_{d,s}T_r\right]n\right\} \\
&\cdot\chi_{LFM}(t - mT_0 - \tau_J, l f_s + f_J + f_{d,s})
\end{aligned}
\tag{32}
$$

$$
\begin{aligned}
r_J(t, f_d) &= \sum_{n=0}^{N-1} r_{J,n}(t)\exp(-j2\pi f_d nT_r) = \\
&A_J\sum_{m=0}^{M-1}\sum_{l=-\infty}^{+\infty} a_l\exp\left(j2\pi(l f_s + f_J)(t - mT_0 - \tau_J) + j2\pi f_{d,s}t\right)\sum_{n=0}^{N-1}\exp\left\{j2\pi\left[\Delta f(t - mT_0 - \tau_J) + (f_{d,s} - f_d)T_r\right]n\right\} \\
&\cdot\chi_{LFM}(t - mT_0 - \tau_J, l f_s + f_J + f_{d,s}) = \\
&A_J\sum_{m=0}^{M-1}\sum_{l=-\infty}^{+\infty} a_l\exp\left\{j2\pi(l f_s + f_J)(t - mT_0 - \tau_J) + j2\pi f_{d,s}t + j\pi\left[\Delta f(t - mT_0 - \tau_J) + (f_{d,s} - f_d)T_r\right](N-1)\right\} \\
&\cdot\frac{\sin\left(\pi\left[\Delta f(t - mT_0 - \tau_J) + (f_{d,s} - f_d)T_r\right]N\right)}{\sin\left(\pi\left[\Delta f(t - mT_0 - \tau_J) + (f_{d,s} - f_d)T_r\right]\right)}\chi_{LFM}(t - mT_0 - \tau_J, l f_s + f_J + f_{d,s})
\end{aligned}
\tag{33}
$$

Since we only consider $|f_d| < 1/(2T_r) < 1/T$, $\chi_{LFM}(t - mT_0 - \tau_J, lf_s + f_J + f_{d,s}) \approx \chi_{LFM}(t - mT_0 - \tau_J, lf_s + f_J + f_{d,s} - f_d)$. Therefore, equation (33) can be rewritten as:

$$r_J(t, f_d)$$

$$\approx A_J \sum_{m=0}^{M-1} \sum_{l=-\infty}^{+\infty} a_l \exp \left\{ \begin{matrix} j2\pi(lf_s + f_J)(t - mT_0 - \tau_J) + j2\pi f_{d,s}t + \\ j\pi \left[\Delta f(t - mT_0 - \tau_J) + (f_{d,s} - f_d)T_r \right](N-1) \end{matrix} \right\}$$

$$\cdot \frac{\sin\left(\pi\left[\Delta f(t - mT_0 - \tau_J) + (f_{d,s} - f_d)T_r\right]N\right)}{\sin\left(\pi\left[\Delta f(t - mT_0 - \tau_J) + (f_{d,s} - f_d)T_r\right]\right)} \quad (34)$$

$$\chi_{LFM}(t - mT_0 - \tau_J, lf_s + f_J + f_{d,s} - f_d) = A_J \psi\left(t - \tau_J, -(f_d - f_{d,s})\right).$$

According to (34), it is clear that the ISRJ can form multiple false targets after RD processing, and these false targets are distributed on the oblique line that passes through the point $(R_{J,m}, f_{d,s})$, where $R_{J,m} = c(\tau_J + mT_0)/2$ and $m = 0, 1, \cdots, M-1$. c denotes speed of light. In addition, the slope of the oblique line is $-k_{\Delta f}$.

4. ISRJ Separation Based on LIFC-LFM Signal Design

4.1 Principle of Interrupted Sampling Repeater Jamming

The analysis in Sec. 3.3 indicates that ISRJ can form multiple false targets after RD processing. These false targets are distributed on the oblique line that passes through the point $(R_{J,m}, f_{d,s})$, where $m = 0,1,\cdots, M-1$. In addition, according to Sec. 2.3, the target echo forms a peak at $(R_s, f_{d,s})$ after the RD processing.

As the ISRJ is formed by jammer sampling and forwarding of the radar signal, $R_{J,m}$ is greater than R_s. Therefore, compared with the LFM pulse train signal, the LIFC-LFM signal can separate true targets from false targets in the RD spectrum. Figure 6 presents an intuitive illustration of the

(a) LFM pulse train signal

(b) LIFC-LFM signal

Fig. 6.   True and false targets in the RD spectrum.

distribution of true and false targets in the RD spectrum. It shows that multiple false targets are horizontally distributed in the RD spectrum when the radar-transmitted signal is an LFM pulse-train signal. These false targets overlapped with the true targets. In contrast, when the transmitted signal is an LIFC-LFM signal, the false targets are obliquely distributed in the RD spectrum and separated from the true target.

In Fig. 6(b), δR_m indicates the range difference corresponding to the delay difference between the target echo and the jamming signal transmitted by the jammer for the m-th time, and $\delta R_m = c(\tau_J + mT_0 - \tau_s)/2$. We denote $\delta\tau_m = \tau_J + mT_0 - \tau_s$ and $\delta R_m = c\delta\tau_m/2$. Additionally, the Doppler interval δf_m satisfies $\delta f_m = -k_{\Delta f}\delta\tau_m$. Therefore, by designing the unit frequency step Δf, the Doppler interval δf_m can be changed to achieve a more effective separation of the true and false targets in the RD spectrum.

4.2 The Design of Unit Frequency Step Δf

In this subsection, we study the design of the unit frequency step Δf. In Sec. 4.1, we introduced that the Doppler interval between the true target and the false target formed by the m-th forwarding jamming signal is $\delta f_m = -k_{\Delta f}\delta\tau_m$. However, because the pulse train signal exhibits periodicity in the Doppler dimension, the calculation method for the Doppler interval is insufficiently accurate. We know that the Doppler period is $1/T_r$, so the Doppler interval δf_m needs to be rewritten as

$$\delta f_m = \begin{cases} \mathrm{mod}\left(-k_{\Delta f}\delta\tau_m, 1/T_r\right) & \left(\mathrm{mod}\left(-k_{\Delta f}\delta\tau_m, 1/T_r\right) \le 1/(2T_r)\right) \\ 1/T_r - \mathrm{mod}\left(-k_{\Delta f}\delta\tau_m, 1/T_r\right) & \left(\mathrm{mod}\left(-k_{\Delta f}\delta\tau_m, 1/T_r\right) > 1/(2T_r)\right) \end{cases} \quad (35)$$

where $\mathrm{mod}(\alpha,\beta) = \alpha - \lceil \alpha/\beta \rceil \cdot \beta$. α and β are the real numbers.

The Doppler correlation corresponding to the Doppler interval δf_m can be expressed as follows

$$\gamma(\delta f_m) = \left| \frac{1}{N} \sum_{n=0}^{N-1} \exp\left(j2\pi\delta f_m nT_r\right) \right| = \left| \frac{1}{N} \frac{\sin(\pi\delta f_m NT_r)}{\sin(\pi\delta f_m T_r)} \right|. \quad (36)$$

The smaller the Doppler correlation between the target echo signal and the ISRJ, the better the separation performance of the ISRJ, and the more conducive it is to the suppression of the ISRJ. When the Doppler interval δf_m satisfies the following equation,

$$\delta f_m = \frac{p}{NT_r} \quad p \in \left\{ -\left\lceil \frac{N}{2} \right\rceil + 1, -\left\lceil \frac{N}{2} \right\rceil + 2, \cdots, \left\lceil \frac{N}{2} \right\rceil \right\} \quad (37)$$

the ISRJ and the target can be considered as completely separated. However, it is difficult to accurately maintain the time delay of ISRJ compared with the target echo, so it is difficult to make (37) hold by designing Δf. From (35), we know that the Doppler interval $\delta f_m \le 1/(2T_r)$. Under this condition, the amplitude of the Doppler correlation function in (36) shows an attenuation trend as δf_m increases. Therefore, we can increase the Doppler interval δf_m as much as possible by designing Δf, which is easy to implement. The optimization problem is established as follows:
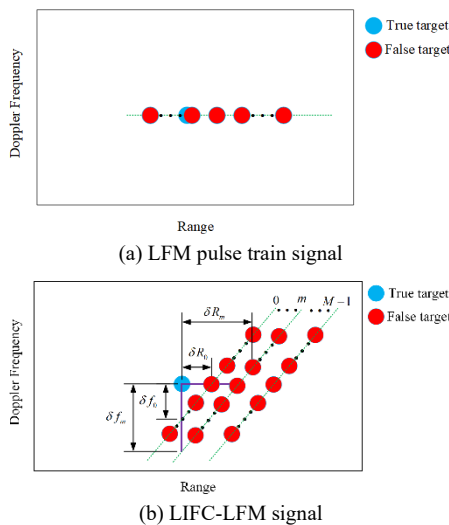
$$\Delta f = \arg\max \min_{\substack{\delta\tau_0 \in \kappa_0 \\ \delta\tau_1 \in \kappa_1 \\ \vdots \\ \delta\tau_{M-1} \in \kappa_{M-1}}} \{\delta f_0, \delta f_1, \cdots, \delta f_{M-1}\}$$

$$\text{s.t. } \Delta f \in \left[-\frac{B}{N}, \frac{B}{N}\right] \tag{38}$$

where κ_m is the value range of $\delta\tau_m$. The constraint condition in (38) is set to alleviate the Doppler mainlobe that broadens the problem of the LIFC-LFM signal. Since ISRJ is generated by a single receive-and-transmit time-sharing antenna, $\tau_J - \tau_s$ is greater than the sampling pulse duration T_0, and it is less than $T_s - T_0$. Therefore, $\kappa_m = [T_0 + mT_0, T_s - T_0]$. We define $\kappa_I = \kappa_0 \cup \kappa_1 \cup \cdots \cup \kappa_{M-1} = [T_0, T_s - T_0]$ and $\delta f = -k_{\Delta f}\delta\tau$, then equation (38) can be rewritten as

$$\Delta f = \arg\max \min_{\delta\tau \in \kappa_I} \delta f$$

$$\text{s.t. } \Delta f \in \left[-\frac{B}{N}, \frac{B}{N}\right] \tag{39}$$

where

$$\delta f = \begin{cases} \mod(-k_{\Delta f}\delta\tau, 1/T_r) & \left(\mod(-k_{\Delta f}\delta\tau, 1/T_r) \le 1/(2T_r)\right) \\ 1/T_r - \mod(-k_{\Delta f}\delta\tau, 1/T_r) & \left(\mod(-k_{\Delta f}\delta\tau, 1/T_r) > 1/(2T_r)\right) \end{cases} \tag{40}$$

Since $\delta f \le 1/(2T_r)$, the optimization problem (39) can be further rewritten as

$$\Delta f = \arg\min \max_{\delta\tau \in \kappa_I} \left(\frac{1}{2T_r} - \delta f\right)$$

$$\text{s.t. } \Delta f \in \left[-\frac{B}{N}, \frac{B}{N}\right]. \tag{41}$$

Finally, we substitute (8) and (40) into (41) and multiply the objective function by a constant T_r. The optimization problem in (41) can be rewritten as

$$\Delta f = \arg\min \max_{\delta\tau \in \kappa_I} \left|\mod(\Delta f \delta\tau, 1) - \frac{1}{2}\right|.$$

$$\text{s.t. } \Delta f \in \left[-\frac{B}{N}, \frac{B}{N}\right]. \tag{42}$$

The optimization problem in (42) can be solved using a linear search. We assume that $\kappa_I = [T_0, T_s - T_0]$ is discretized into G_1 points, and $[-B/N, B/N]$ is discretized into G_2 points. Therefore, the computational complexity is $O(G_1 G_2)$.

In this study, it is assumed that the parameters T_s and T_0 are known and could be estimated using the method proposed in [19].

5. ISRJ Suppression Based on LIFC-LFM Signal Processing

5.1 Range-Doppler Rotation Transformation Based on Fast-time Phase Compensation

The true and false targets in the RD spectrum can be separated by transmitting the LIFC-LFM signal. However, false targets are difficult to suppress because they are obliquely distributed in the RD spectrum and exhibit periodicity in the Doppler dimension. In this section, we propose a range-Doppler rotational transformation method based on phase compensation to solve this problem.

Suppose that there is a target and an ISRJ in the echo. The parameters of the target and ISRJ are the same as those in Sec. 2.3 and 3.3. Without considering the noise, the matching processing result of the echo received in the $(n+1)$-th PRI is expressed as follows:

$$r_n(t) = r_{s,n}(t) + r_{J,n}(t) \approx$$
$$A_s \exp\left(j2\pi f_n(t - \tau_s) + j2\pi f_{d,s}(t + nT_r)\right)\chi_{LFM}(t - \tau_s, 0) +$$
$$A_J \sum_{m=0}^{M-1} \sum_{l=-\infty}^{+\infty} a_l \exp\left(j2\pi(lf_s + f_J)(t - mT_0 - \tau_J) + j2\pi f_{d,s}t\right)$$
$$\exp\left\{j2\pi\left[\Delta f(t - mT_0 - \tau_J) + f_{d,s}T_r\right]n\right\}$$
$$\chi_{LFM}(t - mT_0 - \tau_J, lf_s + f_J + f_{d,s}). \tag{43}$$

To achieve the range-Doppler rotation transformation, we perform fast-time phase compensation for the matching result in (43), and the compensation result is denoted as $\bar{r}_n(t)$:

$$\bar{r}_n(t) = r_n(t)\exp(-j2\pi f_n t) \approx$$
$$A_s \exp(j2\pi f_{d,s}t)\exp\left\{j2\pi\left[-\Delta f\tau_s + f_{d,s}T_r\right]n\right\}\chi_{LFM}(t - \tau_s, 0) +$$
$$A_J \sum_{m=0}^{M-1} \sum_{l=-\infty}^{+\infty} a_l \exp\left(j2\pi(lf_s + f_J)(t - mT_0 - \tau_J) + j2\pi f_{d,s}t\right)$$
$$\exp\left\{j2\pi\left[-\Delta f(mT_0 + \tau_J) + f_{d,s}T_r\right]n\right\}$$
$$\chi_{LFM}(t - mT_0 - \tau_J, lf_s + f_J + f_{d,s}). \tag{44}$$

Furthermore, we performed Doppler coherent processing on the echo received in N PRIs, and the Doppler compensation value was denoted as f_d. The processing result is given in (45).

Equation (45) shows that the Doppler frequency of the true target satisfies $-\Delta f\tau_s + (f_{d,s} - f_d)T_r = 0$, that is, its Doppler frequency is $f_{d,s} - (\Delta f\tau_s)/T_r$. Additionally, the Doppler frequency of the false targets formed by the m-th forwarding jamming signal satisfies $-\Delta f(mT_0 + \tau_J) + (f_{d,s} - f_d)T_r = 0$, and its Doppler frequency is $f_{d,s} - \Delta f(mT_0 + \tau_J)/T_r$. These false targets were shifted to the same Doppler frequency unit using fast-time phase compensation processing. Additionally, true and false targets are separated in the Doppler dimension because they have different Doppler frequencies. The frequency difference between the true target and the false target formed by the m-th forwarding jamming signal is $\Delta f(mT_0 + \tau_J - \tau_s)/T_r = \delta f_m$.

5.2 ISRJ Suppression Based on Oblique Projection Processing

In this section, an oblique projection processing method is used to suppress the ISRJ. First, we stack the matching processing results of the echo received in N PRIs into column vectors, which are denoted as $\bar{r}(t)$ (46).

$$
\bar{r}(t, f_d) = \sum_{n=0}^{N-1} \bar{r}_n(t) \exp(-j2\pi f_d n T_r) \approx
$$

$$
\sum_{n=0}^{N-1} A_s \exp(j2\pi f_{d,s} t) \exp\left\{ j2\pi \left[-\Delta f \tau_s + (f_{d,s} - f_d) T_r \right] n \right\} \chi_{\mathrm{LFM}}(t - \tau_s, 0) +
$$

$$
\sum_{n=0}^{N-1} A_J \sum_{m=0}^{M-1} \sum_{l=-\infty}^{+\infty} a_l \exp\left\{ j2\pi (lf_s + f_J)(t - mT_0 - \tau_J) + j2\pi f_{d,s} t + j2\pi \left[-\Delta f(mT_0 + \tau_J) + (f_{d,s} - f_d) T_r \right] n \right\}
$$

$$
\chi_{\mathrm{LFM}}(t - mT_0 - \tau_J, lf_s + f_J + f_{d,s}) = \tag{45}
$$

$$
A_s \exp\left\{ j2\pi f_{d,s} t + j\pi \left[-\Delta f \tau_s + (f_{d,s} - f_d) T_r \right] (N-1) \right\} \frac{\sin\left(\pi \left[-\Delta f \tau_s + (f_{d,s} - f_d) T_r \right] N \right)}{\sin\left(\pi \left[-\Delta f \tau_s + (f_{d,s} - f_d) T_r \right] \right)} \chi_{\mathrm{LFM}}(t - \tau_s, 0) +
$$

$$
A_J \sum_{m=0}^{M-1} \sum_{l=-\infty}^{+\infty} a_l \exp\left\{ j2\pi (lf_s + f_J)(t - mT_0 - \tau_J) + j2\pi f_{d,s} t + j\pi \left[-\Delta f(mT_0 + \tau_J) + (f_{d,s} - f_d) T_r \right] (N-1) \right\}
$$

$$
\frac{\sin\left(\pi \left[-\Delta f(mT_0 + \tau_J) + (f_{d,s} - f_d) T_r \right] N \right)}{\sin\left(\pi \left[-\Delta f(mT_0 + \tau_J) + (f_{d,s} - f_d) T_r \right] \right)} \chi_{\mathrm{LFM}}(t - mT_0 - \tau_J, lf_s + f_J + f_{d,s}),
$$

$$
\bar{\boldsymbol{r}}(t) = \begin{bmatrix} \bar{r}_0(t) & \bar{r}_1(t) & \cdots & \bar{r}_{N-1}(t) \end{bmatrix}^{\mathrm{T}} =
$$

$$
\begin{bmatrix} \exp\left(j2\pi (-\Delta f \tau_s + f_{d,s} T_r) 0 \right), \cdots, \exp\left(j2\pi (-\Delta f \tau_s + f_{d,s} T_r)(N-1) \right) \end{bmatrix}^{\mathrm{T}} A_s \exp(j2\pi f_{d,s} t) \chi_{\mathrm{LFM}}(t - \tau_s, 0) +
$$

$$
\sum_{m=0}^{M-1} \begin{bmatrix} \exp\left\{ j2\pi \left[-\Delta f(mT_0 + \tau_J) + f_{d,s} T_r \right] 0 \right\}, \cdots, \exp\left\{ j2\pi \left[-\Delta f(mT_0 + \tau_J) + f_{d,s} T_r \right] (N-1) \right\} \end{bmatrix}^{\mathrm{T}}
$$

$$
\sum_{l=-\infty}^{+\infty} A_{m,l}(t) \chi_{\mathrm{LFM}}(t - mT_0 - \tau_J, lf_s + f_J + f_{d,s}) = \tag{46}
$$

$$
\boldsymbol{b}\left(-\Delta f \frac{\tau_s}{T_r} + f_{d,s} \right) A_s \exp(j2\pi f_{d,s} t) \chi_{\mathrm{LFM}}(t - \tau_s, 0) +
$$

$$
\sum_{m=0}^{M-1} \boldsymbol{b}\left(-\Delta f \frac{mT_0 + \tau_J}{T_r} + f_{d,s} \right) \sum_{l=-\infty}^{+\infty} A_{m,l}(t) \chi_{\mathrm{LFM}}(t - mT_0 - \tau_J, lf_s + f_J + f_{d,s})
$$

where

$$
A_{m,l}(t) = A_J a_l \exp\left(j2\pi (lf_s + f_J)(t - mT_0 - \tau_J) + j2\pi f_{d,s} t \right) \tag{47}
$$

and

$$
\boldsymbol{b}(f_d) = \begin{bmatrix} \exp(j2\pi f_d 0 T_r), \cdots, \exp(j2\pi f_d (N-1) T_r) \end{bmatrix}^{\mathrm{T}} \tag{48}
$$

Therefore, the Doppler vector space of the true and false targets can be denoted as $\boldsymbol{U}_s = [\boldsymbol{b}(-(\Delta f \tau_s)/T_r + f_{d,s})]$ and $\boldsymbol{U}_J = [\boldsymbol{b}(-\Delta f(0T_0 + \tau_J)/T_r + f_{d,s}), \quad \boldsymbol{b}(-\Delta f(1T_0 + \tau_J)/T_r + f_{d,s}), \quad \cdots, \boldsymbol{b}(-\Delta f[(M-1)T_0 + \tau_J]/T_r + f_{d,s})]$. Notably, we can obtain the Doppler frequency information of true and false targets by performing super-resolution processing on $\bar{\boldsymbol{r}}(t)$. The super-resolution algorithm adopted in this study was the multiple signal classification (MUSIC) algorithm. The specific processing of the MUSIC algorithm can be found in [36].

Furthermore, we can establish the oblique projection matrix $\boldsymbol{E}_{[U_s, U_J]}$,

$$
\boldsymbol{E}_{[U_s, U_J]} = \boldsymbol{U}_s \left[\boldsymbol{U}_s^{\mathrm{H}} \boldsymbol{P}_{U_J}^{\perp} \boldsymbol{U}_s \right]^{-1} \boldsymbol{U}_s^{\mathrm{H}} \boldsymbol{P}_{U_J}^{\perp} \tag{49}
$$

where $\boldsymbol{P}_{U_J}^{\perp}$ represents the orthogonal complement projection matrix of the subspace $\boldsymbol{U}_J$,

$$
\boldsymbol{P}_{U_J}^{\perp} = \boldsymbol{I}_N - \boldsymbol{U}_J \left(\boldsymbol{U}_J^{\mathrm{H}} \boldsymbol{U}_J \right)^{-1} \boldsymbol{U}_J^{\mathrm{H}}. \tag{50}
$$

The established matrix $\boldsymbol{E}_{[U_s, U_J]}$ is endowed with the properties $\boldsymbol{E}_{[U_s, U_J]} \boldsymbol{U}_s = \boldsymbol{U}_J$ and $\boldsymbol{E}_{[U_s, U_J]} \boldsymbol{b}(-\Delta f(mT_0 + \tau_J)/T_r + f_{d,s})$

$= 0$. We performed oblique projections on $\bar{\boldsymbol{r}}(t)$, and the processing result of $\bar{\boldsymbol{y}}(t)$ is expressed as follows:

$$
\bar{\boldsymbol{y}}(t) = \boldsymbol{E}_{[U_s, U_J]} \bar{\boldsymbol{r}}(t) =
$$

$$
\boldsymbol{U}_s \left[\boldsymbol{U}_s^{\mathrm{H}} \boldsymbol{P}_{U_J}^{\perp} \boldsymbol{U}_s \right]^{-1} \boldsymbol{U}_s^{\mathrm{H}} \boldsymbol{P}_{U_J}^{\perp} \boldsymbol{U}_s A_s \exp(j2\pi f_{d,s} t) \chi_{\mathrm{LFM}}(t - \tau_s, 0) +
$$

$$
\sum_{m=0}^{M-1} \boldsymbol{U}_s \left[\boldsymbol{U}_s^{\mathrm{H}} \boldsymbol{P}_{U_J}^{\perp} \boldsymbol{U}_s \right]^{-1} \boldsymbol{U}_s^{\mathrm{H}} \boldsymbol{P}_{U_J}^{\perp} \boldsymbol{b}\left(-\Delta f \frac{mT_0 + \tau_J}{T_r} + f_{d,s} \right) = \tag{51}
$$

$$
\sum_{l=-\infty}^{+\infty} A_{m,l}(t) \chi_{\mathrm{LFM}}(t - mT_0 - \tau_J, lf_s + f_J + f_{d,s})
$$

$$
\boldsymbol{U}_s A_s \exp(j2\pi f_{d,s} t) \chi_{\mathrm{LFM}}(t - \tau_s, 0) =
$$

$$
\begin{bmatrix} r_{s,0}(t) \exp(-j2\pi f_0 t), \cdots, r_{s,N-1}(t) \exp(-j2\pi f_{N-1} t) \end{bmatrix}^{\mathrm{T}}.
$$

The above equation shows that oblique projection can effectively filter the ISRJ. Since fast-time phase compensation changes the Doppler frequency of the true target, we need to perform inverse phase compensation on the oblique projection processing results. The inverse-phase compensation result is denoted as $\boldsymbol{y}(t)$

$$
\boldsymbol{y}(t) = \begin{bmatrix} e^{j2\pi f_0 t} & 0 & 0 \\ 0 & \ddots & 0 \\ 0 & 0 & e^{j2\pi f_{N-1} t} \end{bmatrix} \bar{\boldsymbol{y}}(t) = \tag{52}
$$

$$
\begin{bmatrix} r_{s,0}(t) & r_{s,1}(t) & \cdots & r_{s,N-1}(t) \end{bmatrix}^{\mathrm{T}}.
$$

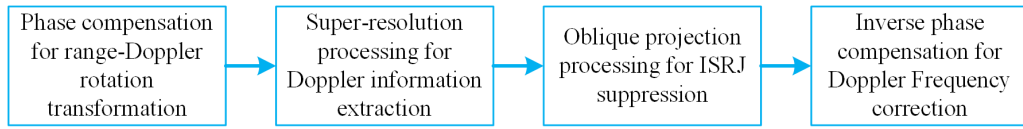| Phase compensation for range-Doppler rotation transformation	→	Super-resolution processing for Doppler information extraction	→	Oblique projection processing for ISRJ suppression	→	Inverse phase compensation for Doppler Frequency correction

Fig. 7. ISRJ suppression processing process.

Finally, we performed Doppler coherent processing on $y(t)$, and the Doppler compensation value is denoted as f_d. The processing result is

$$r(t,f_d) = \sum_{n=0}^{N-1} r_{s,n}(t)\exp(-j2\pi f_d(nT_r))$$

$$= A_s \exp\left\{ j2\pi f_{d,s}t + j\pi\left[\Delta f(t-\tau_s) + (f_{d,s}-f_d)T_r \right](N-1) \right\} \quad (53)$$

$$\cdot \frac{\sin\left\{ N\pi\left[\Delta f(t-\tau_s) + (f_{d,s}-f_d)T_r \right] \right\}}{\sin\left\{ \pi\left[\Delta f(t-\tau_s) + (f_{d,s}-f_d)T_r \right] \right\}} \chi_{LFM}(t-\tau_s,0).$$

It can be observed that false targets are suppressed. Additionally, the true target outputs a peak at $(\tau_s, f_{d,s})$. The ISRJ suppression process is illustrated in Fig. 7.

6. Numerical Simulation

In this section, we verify the effectiveness of the proposed ISRJ suppression method through simulation experiments. The simulation parameters of the radar system and sampling function $p(t)$ are listed in Tab. 1 unless otherwise specified. We adopted the Hamming window function for range sidelobe suppression, and the specific method involved multiplying the reference signal used for matching processing with the Hamming window function as the new reference signal.

6.1 Range-Doppler Spectrum Analysis

Compared with the LFM pulse train signal, the LIFC-LFM signal can cause false targets formed by the ISRJ to distribute obliquely in the RD spectrum, thus realizing the separation of true and false targets. This section presents three intuitive examples that demonstrate this property. Furthermore, we provide the RD spectrum obtained at each step of the proposed ISRJ suppression method. According to the parameters set in Tab. 1, we can calculate $|\Delta f| = 390.6$ kHz by (42). We set Δf as 390.6 kHz, thus the slope of the distribution of false targets in the RD spectrum is $-2k_{\Delta f}/c = 26.04$.
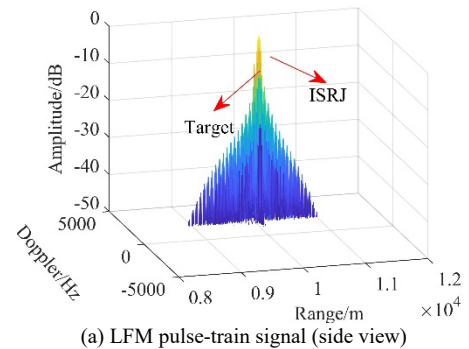
(1) Direct forwarding ISRJ ($M = 1, f_J = 0$ Hz)

The target was located 10 km away at a velocity of 300 m/s. It was equipped with a self-defense jammer that generated an ISRJ by transmitting the sampled signal once. The time delay of the ISRJ with respect to the target echo is 0.5 µs. Figure 8 illustrates the RD spectrum of the echo. In Figs. 8(a) and 8(c), we consider the case of the radar transmitting the LFM pulse train signal and the LIFC-LFM signal, respectively. Additionally, Figures 8(b) and 8(d) show top views of Figs. 8(a) and 8(c), respectively. It can be observed from Figs. 8(a) and 8(b) that the false targets obscure the true target in the RD spectrum. In contrast, because the LIFC-LFM signal can cause the false targets to be distributed obliquely in the RD spectrum, the false targets can be separated from the true target, as shown in Figs. 8(c) and 8(d). The range interval between the true target and main false target is 75 m, where the main false target refers to the false target located at the center. The Doppler interval between the true and false targets in the same range unit is approximately 1952.7 Hz. We calculated that the slope of the oblique distribution of false targets in the RD spectrum is approximately 26.036, which is close to $-2k_{\Delta f}/c$.

As shown in Fig. 8(d), the false targets are obliquely distributed in the RD spectrum and exhibit periodicity in the Doppler dimension, which is inconducive to ISRJ suppression. The problem can be solved using the range-Doppler
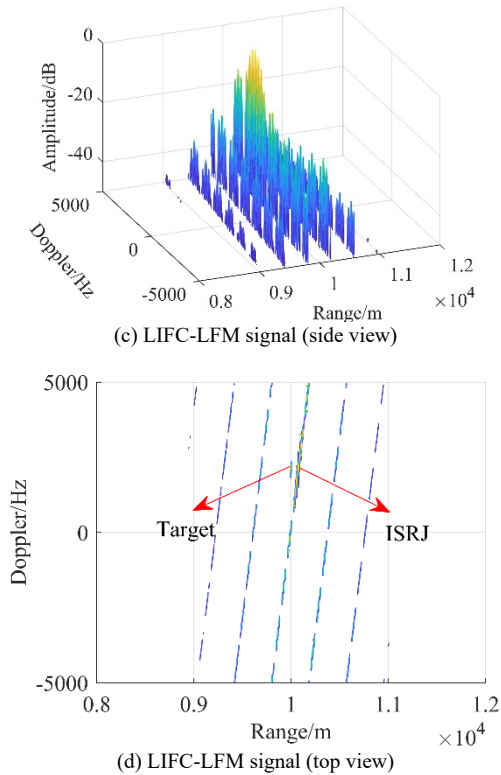
Parameter	Value
PRI	100 µs
Pulse width	10 µs
Coherent pulse number	128
Bandwidth	50 MHz
Carrier frequency	1 GHz
Sampling pulse duration	0.5 µs
Sampling period	2 µs
Signal to interference ratio (SIR)	−20 dB

Tab. 1. Simulation parameters of the radar system and interrupted sampling signal.

(a) LFM pulse-train signal (side view)

(b) LFM pulse train signal (top view)

(c) LIFC-LFM signal (side view)

(d) LIFC-LFM signal (top view)

Fig. 8. Range-Doppler processing results of direct forwarding ISRJ ($M = 1$, $f_J = 0$ Hz).

rotation-transformation method. The echo of the LIFC-LFM signal was processed using the method proposed in Sec. 5. The direct forwarding of the ISRJ suppression process is illustrated in Fig. 9.
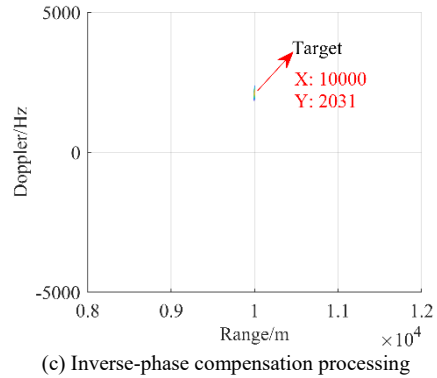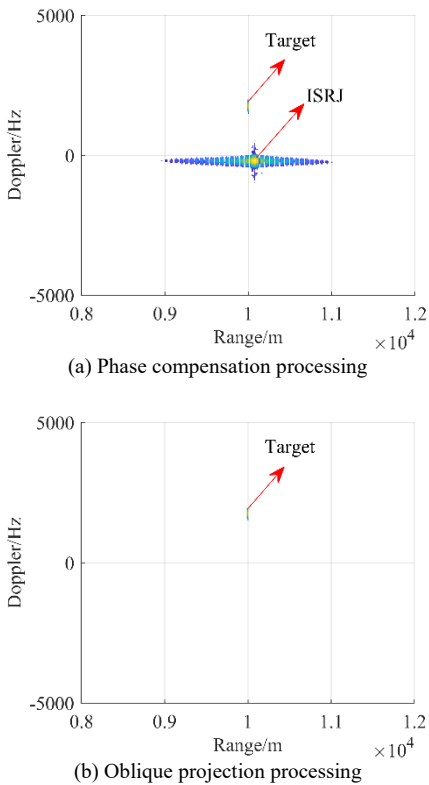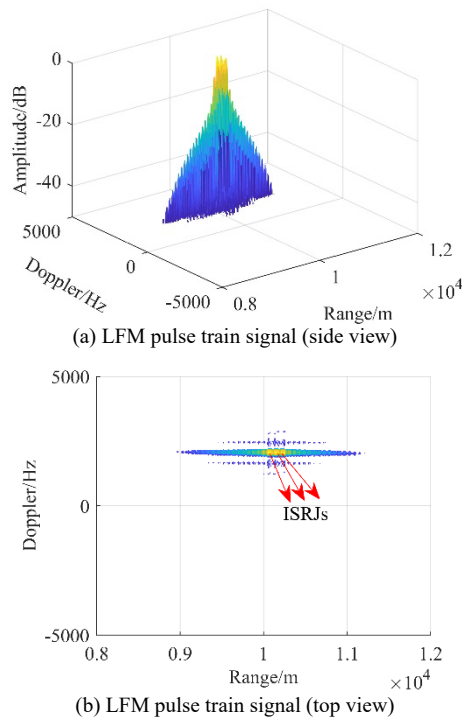

(a) Phase compensation processing

(b) Oblique projection processing

(c) Inverse-phase compensation processing

Fig. 9. Direct forwarding ISRJ suppression processing process ($M = 1$, $f_J = 0$ Hz).

Figure 9(a) shows that all the false targets moved to the same Doppler unit in the RD spectrum after the range-Doppler rotation transformation. These were effectively separated from the true target in the Doppler dimension. Furthermore, false targets can be suppressed using oblique projection processing, as shown in Fig. 9(b). Upon achieving false-target suppression, we performed inverse phase compensation on the oblique projection processing results to correct the Doppler frequency of the true target, as shown in Fig. 9(c). This shows that false targets are effectively suppressed, and the true target can be correctly detected.

(2) Repeated forwarding ISRJ ($M = 3$, $f_J = 0$ Hz)

The target was located 10 km away at a velocity of 300 m/s. It was equipped with a self-defense jammer that generated an ISRJ by transmitting the sampled signal three times. Compared with the target echo, the time delays of three forwarding of the jamming signal are 0.5 μs, 1 μs, and 1.5 μs, respectively. Figure 10 illustrates the RD spectrum

(a) LFM pulse train signal (side view)

(b) LFM pulse train signal (top view)

(c) LIFC-LFM signal (side view)

(d) LIFC-LFM signal (top view)
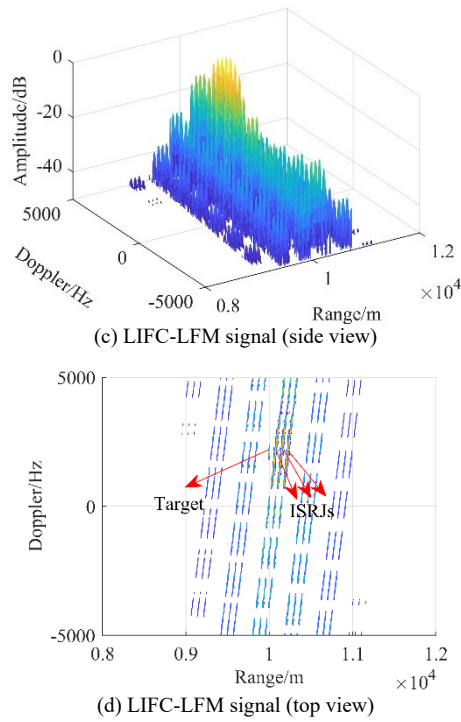
Fig. 10. Range-Doppler processing results of repeated forwarding ISRJ ($M = 3$, $f_J = 0$ Hz).

of the echo after RD processing. The LIFC-LFM signal can still separate true and false targets in the RD spectrum.

Figure 11 illustrates the RD spectrum after each step of the repeated forward ISRJ suppression. In Fig. 11(a), the RD spectrum of the echo after the range-Doppler rotation transformation is shown. Evidently, the false targets are moved to three different Doppler units, which is owing to the fact

(a) Phase compensation processing

(b) Oblique projection processing

(c) Inverse-phase compensation processing
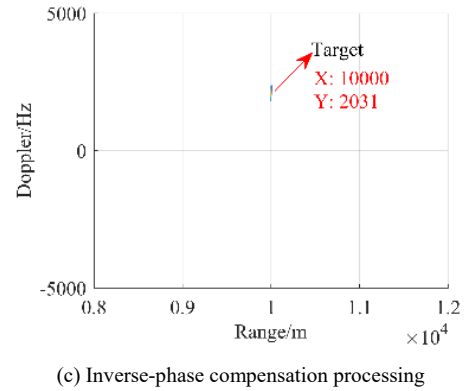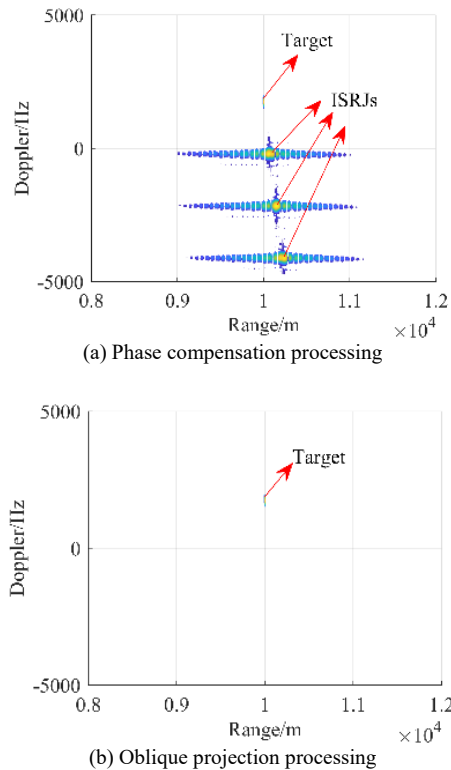
Fig. 11. Repeated forwarding ISRJ suppression processing process ($M = 3$, $f_J = 0$ Hz).

that the repeated forwarding ISRJ can be considered as the sum of three direct forwarding ISRJ with different time shifts. Furthermore, false targets are effectively suppressed by oblique projection processing, as shown in Fig. 11(b). Finally, inverse phase compensation was performed to correct the Doppler frequency of the true target.

(3) Frequency shifting ISRJ ($M = 1$, $f_J = 6$ MHz)

The target was located 10 km away with a velocity of 300 m/s and was equipped with a self-defense jammer. The jammer modulates the sampled signal with a frequency shift of 6 MHz and forwards it once to form a frequency-shifting ISRJ. The time delay of the ISRJ compared with the target echo is 0.5 μs. Figure 12 illustrates the RD spectrum of the echo after RD processing. Unlike the main false target formed by the direct forwarding ISRJ, which lags behind the true target, the frequency-shifting ISRJ can control the distance position of the main false target when the radar-transmitted signal is the LFM pulse train signal. As shown in Fig. 12(a) and (b), the main false target is located before the
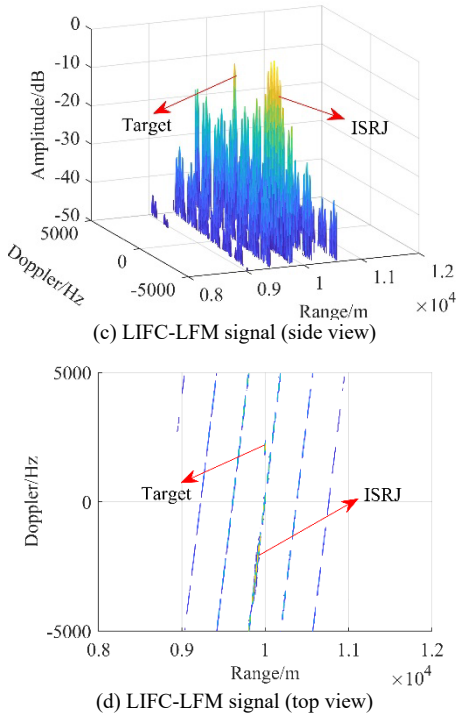

(a) LFM pulse train signal (side view)

(b) LFM pulse train signal (top view)

(c) LIFC-LFM signal (side view)

(d) LIFC-LFM signal (top view)
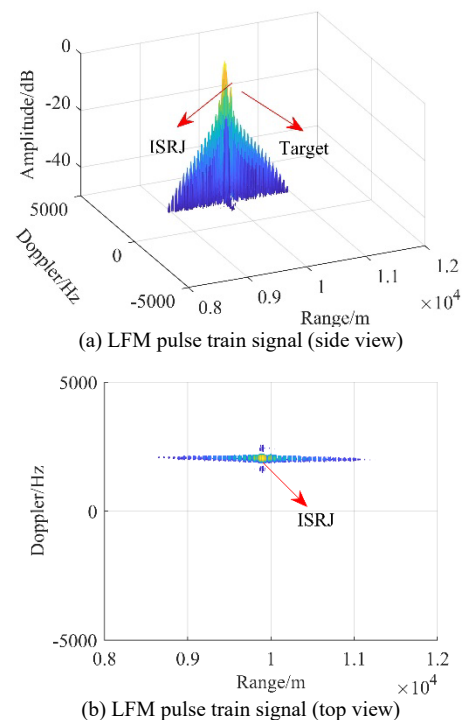
Fig. 12. Range-Doppler processing results of frequency shifting ISRJ ($M = 1$, $f_J = 6$ MHz).

true target distance unit. In contrast, this characteristic does not affect the validity of our proposed method because the frequency-shifting ISRJ can only make the false targets move obliquely on the oblique line where they are located, as shown in Figs. 12(c) and (d). We can still achieve the separation of true and false targets by transmitting the LIFC-LFM signal. The Doppler interval between the true and false targets located in the same range unit was also approximately 1952.7 Hz.

(a) Phase compensation processing

(b) Oblique projection processing

(c) Inverse phase compensation processing
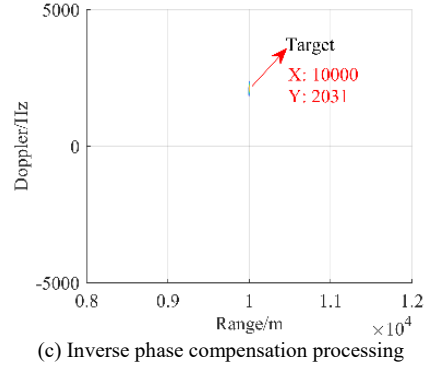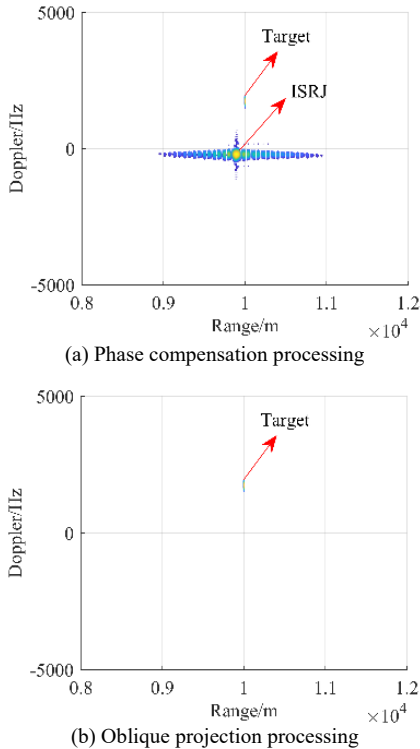
Fig. 13. Frequency shifting ISRJ suppression processing process ($M = 1$, $f_J = 6$ MHz).

Figure 13 illustrates the RD spectrum after each step of the frequency-shifting ISRJ suppression. It is demonstrated that the frequency-shifting ISRJ can be effectively suppressed.

The above three examples prove that the proposed method can effectively separate and suppress three different ISRJs: the direct forwarding ISRJ, repeated forwarding ISRJ, and frequency-shifting ISRJ.

6.2 Unit Frequency Step Δ*f* Value Analysis

In this subsection, we first verify the effectiveness of the unit frequency step Δf design method proposed in Sec. 4.2, and then analyze the influence of the unit frequency step Δf value on SNR loss and Doppler broadening.

(1) The influence of Δf on ISRJ separation

The time delay $\delta\tau$ of the ISRJ compared with the target echo is greater than the sampling pulse duration $T_0 = 0.5$ μs, and is smaller than $T_s - T_0 = 1.5$ μs. Additionally, the unit frequency step should satisfy $|\Delta f| \leq 390.6$ kHz according to (10). Since the positive or negative value of Δf has the same jamming separation effect, we only consider the case where Δf takes the positive number. Figure 14 shows the influence of unit frequency step Δf on Doppler interval. In Fig. 14(a), the relationship between the time delay $\delta\tau$ and the Doppler interval under different Δf is plotted. It can be observed that the minimum value of the red line is the largest. The unit frequency step Δf corresponding to the red line is 390.6 kHz, which is the optimal value calculated by (42). Furthermore, Figure 14(b) illustrates the relationship between the unit fre-
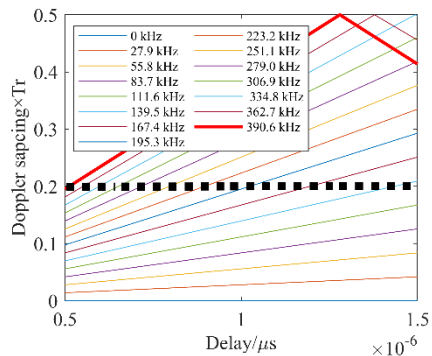
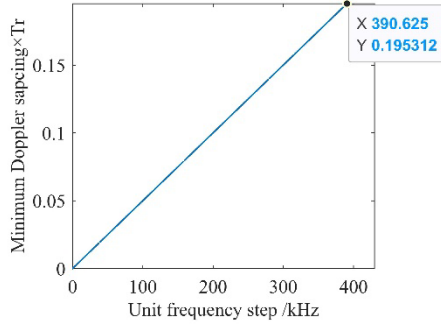(a) Relationship between $\delta\tau$ and Doppler interval

(b) Relationship between *f* and minimum Doppler interval

Fig. 14. Influence of unit frequency step Δf value on Doppler interval.

quency step Δf and the minimum Doppler interval. This shows that the step factor calculated using (42) can separate true and false targets more effectively.

(2) The influence of Δf on SNR loss

In Sec. 5.2, we suppress ISRJ using oblique projection processing, which leads to SNR loss. The SNR loss was calculated using the following equation:

$$\text{SNR}_{\text{loss}} = \frac{\text{SNR}_{\text{Before}}}{\text{SNR}_{\text{After}}} \qquad (54)$$

where $\text{SNR}_{\text{Before}}$ indicates the output SNR before oblique projection processing,

$$\text{SNR}_{\text{Before}} = \frac{\sigma_s^2 \left(U_s^H U_s \right)^2}{U_s^H N_w N_w^H U_s} \qquad (55)$$

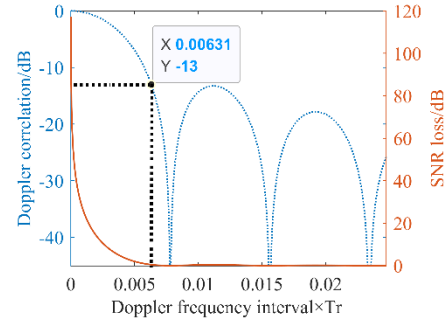and $\text{SNR}_{\text{After}}$ refers to the output SNR after oblique projection processing,

$$\text{SNR}_{\text{After}} = \frac{\sigma_s^2 \left| U_s^H E_{[U_s, U_J]} U_s \right|^2}{\left(U_s^H E_{[U_s, U_J]} N_w \right) \left(U_s^H E_{[U_s, U_J]} N_w \right)^H} . \qquad (56)$$

In (55) and (56), N_w represents white noise and satisfies the $N_w N_w^H = \sigma_w^2 I_N$. σ_s^2 and σ_w^2 represent the powers of the true target and noise, respectively. Accordingly, (54) can be rewritten as

$$\text{SNR}_{\text{loss}} = \frac{U_s^H E_{[U_s, U_J]} E_{[U_s, U_J]}^H U_s}{U_s^H U_s} . \qquad (57)$$
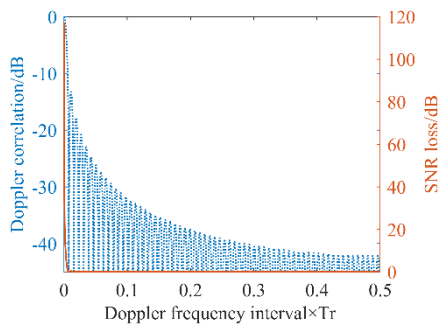
(a) Total graph

Fig. 15. Relationship between Doppler correlation and SNR loss.

(b) Partially enlarged detail

Figure 15 presents the simulation results of the relationship between the Doppler correlation and the SNR loss, where Figure 15(b) shows a partially enlarged detail of Fig. 15(a). As depicted in the figure, the Doppler correlation exhibits an attenuation trend with an increase in the Doppler interval, and the SNR loss decreases gradually. When the Doppler interval exceeds 63.1 Hz, the Doppler correlation is less than –13 dB, and the SNR loss is close to 0 dB. According to the simulation results shown in Fig. 14 and Fig. 15, the proposed method is expected to achieve ISRJ suppression with small SNR loss.

(3) The influence of Δf on Doppler mainlobe broadening

In Sec. 2.2, we introduce the fact that the AF of the LIFC-LFM signal has a range-Doppler coupling effect.

(a) $\Delta f = 0$ kHz

(b) $\Delta f = 195.3$ kHz

(c) $\Delta f = 390.6$ kHz

(d) $\Delta f = 781.2$ kHz

(e) $\Delta f = 1953$ kHz

(f) $\Delta f = 3906$ kHz
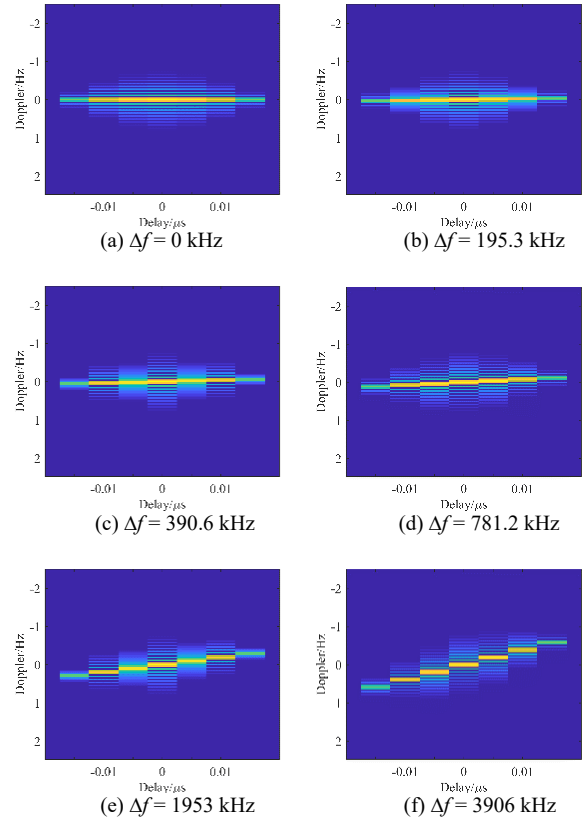
Fig. 16. Influence of Δf on Doppler mainlobe broadening.

Therefore, the Doppler mainlobe width of the LIFC-LFM signal AF may be broadened when Δf is large. This conclusion was verified through a simulation experiment. In Fig. 16, we present the AF of the LIFC-LFM signal corresponding to different values of Δf. For ease of analysis, the display range of the delay axis is $[-0.02, +0.02]$ μs, which corresponds to the delay mainlobe region. It can be observed from the figure that the mainlobe of the ambiguity function is obliquely distributed when $\Delta f \neq 0$ Hz, and the slope gradually increases as Δf increases. This broadens the ambiguity function of the Doppler mainlobe. Therefore, we design Δf in Sec. 4.2 with a constraint on the value range of Δf, thus alleviating the Doppler broadening problem. The simulations prove the effectiveness of the proposed unit frequency step design method.

6.3 ISRJ Suppression Performance Analysis

In this section, the anti-jamming performance of the proposed method is simulated and verified. We compared it with the LFM pulse train signal, the method proposed in [21], and the method proposed in [24]. We conducted three sets of experiments: influence analysis of the input SIR, influence analysis of the jamming parameter estimation error, and influence analysis of the jamming frequency shift modulation. Since repeated forwarding ISRJ can be regarded as the sum of multiple direct-forwarding ISRJ with different delays, we set jamming in the echo as repeated forwarding ISRJ in the first two experiments. Unless otherwise specified, the simulation parameters are the same as those in the second example in Sec. 6.1. In the third group of experiments, we studied the suppression performance of the four methods on the frequency-shifting ISRJ. The simulation parameters are the same as those in the third example in Sec. 6.1, except for the frequency-shift modulation value and input SIR.

(1) Influence of input SIR

First, we demonstrate the effect of the input SIR on the anti-jamming performance of the four methods. As shown in Fig. 17, the output SIR of the first three methods are linearly related to the input SIR. This phenomenon occurred because the LFM pulse train signal could not resist the ISRJ. Moreover, the ISRJ suppression performance of the method proposed in [21] depends on the orthogonality of the designed sub-signals. Similarly, the performance of the method proposed in [24] is based on the orthogonality between the designed waveform and mismatched filter. In comparison, our proposed method can suppress jamming to the bottom of the noise; therefore, the output SIR in the figure is related to the input SNR, but not to the input SIR. This shows that the proposed method has a better ISRJ suppression performance.

We set the input SIR to -20 dB and present the range spectrum of the echo processing output of four methods, as shown in Fig. 18. In Fig. 18, because the LFM pulse train signal cannot suppress ISRJ, its output SINR is approximately -9.1 dB. The output SIR of the method proposed in [21] is approximately -0.99 dB. This method can weaken the ISRJ energy; however, its anti-jamming performance is
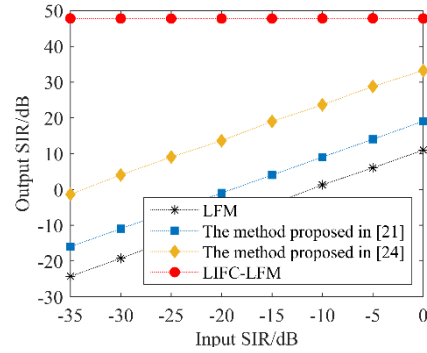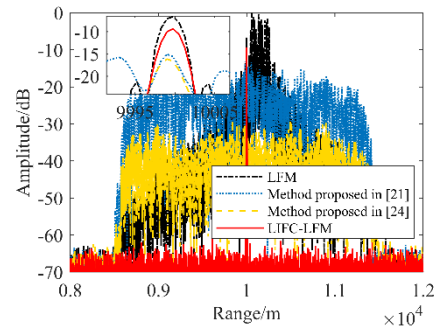

Fig. 17. Influence of input SIR.

Fig. 18. Range spectrum of the echo processing output.

poor when the jamming amplitude is large. By contrast, the method proposed in [24] can effectively improve the ISRJ suppression performance through the joint design of the waveform and mismatch filter, whose output SIR is approximately 13.63 dB. However, this method requires a complex waveform and filter design. Additionally, considering the SNR loss requirement, it is difficult to suppress the ISRJ at the bottom of the noise. The output SIR of the proposed method is approximately 53.77 dB. Jamming was suppressed at the bottom of the noise, and the SNR loss was smaller. It can be observed that the proposed method exhibits better ISRJ suppression performance.

(2) Influence of jamming parameter estimation error

The methods proposed in [21], [24] and our proposed method must estimate the ISRJ parameters before designing the waveform. In the above experiments, we simulated under ideal conditions; that is, the ISRJ parameters were accurately estimated. In this section, we analyze the influence of jamming parameter estimation error on anti-jamming performance. Two jamming parameters need to be estimated: the sampling pulse duration and sampling period. In the simulation, the input SIR is set to -10 dB. Figure 19 illustrates the relationship between the output SIR and sampling pulse duration estimation error. The anti-jamming performance of the method proposed in [24] decreases as the sampling period estimation error increases. In contrast, the methods proposed in [21] and the method proposed in this study are almost unaffected. This is because the proposed method can still separate true and false targets when there exists a certain error in the estimation of the sampling pulse duration, and the condition that the Doppler interval is greater than 63.1 Hz can be easily satisfied.
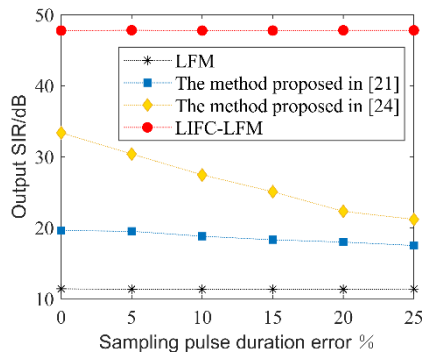
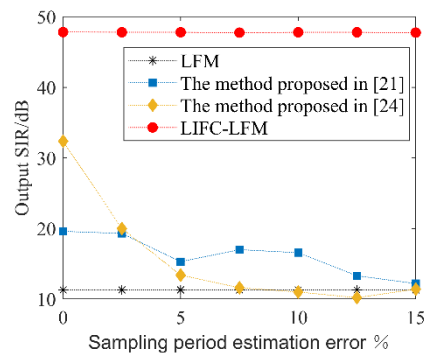**Fig. 19.** Influence of sampling pulse duration estimation error.

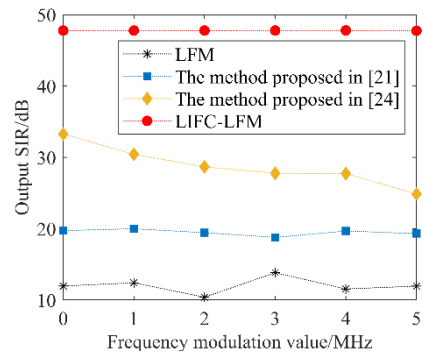**Fig. 20.** Influence of sampling period estimation error.

Fig. 21. Influence of frequency shift modulation.

Figure 20 depicts the relationship between the output SIR and sampling period estimation error. The anti-jamming performance of the methods proposed in [21] and [24] decreases with an increase in the sampling period estimation error. The anti-jamming performance of the method proposed in [24] was significantly reduced. In contrast, the proposed method is almost unaffected, and the reason is the same as above.

The simulations in this section showed that our proposed method has a more robust ISRJ suppression effect and is less dependent on the accuracy of the jamming parameter estimation.

(3) Effect of frequency shift modulation

Finally, we considered the suppression performances of the four methods for the frequency-shifting ISRJ. In the simulation, the input SIR was set to −10 dB, and the jamming parameters were estimated accurately. The simulation results are presented in Fig. 21. In the figure, the output SIR

of the methods proposed in [24] decreases as the frequency modulation value increases. In comparison, the proposed method is less sensitive to changes in frequency modulation value. This phenomenon occurs because the proposed method has the same separation performance for frequency-shifting ISRJ as for ISRJ without frequency modulation.

7. Conclusions

In this study, we propose an ISRJ suppression method based on LIFC-LFM signal design and processing. The proposed LIFC-LFM signal can separate true and false targets in the RD spectrum. Based on the target echo signal and ISRJ echo analysis, the principle of ISRJ separation was revealed at the design stage, and an LIFC-LFM design method was devised. Furthermore, an ISRJ filtering method was developed based on the range-Doppler rotation transformation and oblique projection. In the analysis stage, simulation examples demonstrate that the proposed method has excellent ISRJ suppression performance for direct forwarding ISRJ, repeated forwarding ISRJ, and frequency-shifting ISRJ. Additionally, it has a robust ISRJ suppression performance, and the anti-jamming performance is less affected by the input SIR and estimation error of the ISRJ parameters.

Acknowledgments

References

[1] ROOME, S. Digital radio frequency memory. *Electronics & Communications Engineering Journal,* 1990, vol. 47, no. 14, p. 147 to 153. DOI: 10.1049/ecej:19900035

[2] OLIVIER, K., CILLIERS, J. E., DU PLESSIS M. Design and performance of wideband DRFM for radar test and evaluation. *Electronics Letters,* 2011, vol. 2, no. 4, p. 824–825. DOI: 10.1049/EL.2011.0362

[3] WANG, X., LIU, J., ZHANG, W., et al. Mathematic principles of interrupted-sampling repeater jamming (ISRJ). *Science in China Series F: Information Sciences,* 2007, vol. 50, p. 113–123. DOI: 10.1007/s11432-007-2017-y

[4] FENG, D., XU, L., PAN, X., et al. Jamming wideband radar using interrupted-sampling repeater. *IEEE Transactions on Aerospace and Electronic Systems,* 2017, vol. 53, no. 3, p. 1341–1354. DOI: 10.1109/TAES.2017.2670958

[5] BAHER SAFA HANBALI, S. Technique to counter improved active echo cancellation based on ISRJ with frequency shifting. *IEEE Sensors Journal,* 2019, vol. 19, no. 20, p. 9194–9199. DOI: 10.1109/JSEN.2019.2925004

[6] SOUMEKH, M. SAR-ECCM using phase-perturbed LFM chirp signals and DRFM repeat jammer penalization. In *IEEE*

International Radar Conference. Arlington (VA, USA), 2005, p. 507–512. DOI: 10.1109/RADAR.2005.1435879

[7] SOUMEKH, M. SAR-ECCM using phase-perturbed LFM chirp signals and DRFM repeat jammer penalization. *IEEE Transactions on Aerospace and Electronic Systems,* 2006, vol. 42, no. 1, p. 191 to 205. DOI: 10.1109/TAES.2006.1603414

[8] AKHTAR, J. An ECCM scheme for orthogonal independent range-focusing of real and false targets. In *IEEE Radar Conference.* Waltham (MA, USA), 2007, p. 846–849. DOI: 10.1109/RADAR.2007.374330

[9] AKHTAR, J. Orthogonal block coded ECCM schemes against repeat radar jammers. *IEEE Transactions on Aerospace and Electronic Systems,* 2009, vol. 45, no. 3, p. 1218–1226. DOI: 10.1109/TAES.2009.5259195

[10] ZHANG, J., ZHU, D., ZHANG, G. New antivelocity deception jamming technique using pulses with adaptive initial phases. *IEEE Transactions on Aerospace and Electronic Systems,* 2013, vol. 49, no. 2, p. 1290–1300. DOI: 10.1109/TAES.2013.6494414

[11] DAI, J., HAO, X., LIU, Q., et al. Repeater jamming suppression method for pulse Doppler fuze based on identity recognition and chaotic encryption. *Defence Technology,* 2021, vol. 17, no. 3, p. 1002–1012. DOI: 10.1016/j.dt.2020.06.023

[12] LIU, S., LI, B., ZHAO, B., et al. A super resolution target separation and reconstruction approach for single channel SAR against deceptive jamming. *Defence Technology,* 2023, vol. 21, p. 164–175. DOI: 10.1016/j.dt.2021.10.008

[13] LAN, L., LIAO, G., XU, J., et al. Mainlobe deceptive jammer suppression using element-pulse coding with MIMO radar. *Signal Processing,* 2021, vol. 182, p. 1–14. DOI: 10.1016/j.sigpro.2020.107955

[14] LAN, L., LIAO, G., XU, J., et al. Mainlobe deceptive jammer suppression with MIMO radar using element-pulse coding. In *IEEE Radar Conference.* Florence (Italy), 2020, p. 1–6. DOI: 10.1109/RadarConf2043947.2020.9266390

[15] GONG, S., WEI, X., LI, X. ECCM scheme against interrupted sampling repeater jammer based on time-frequency analysis. *Journal of Systems Engineering and Electronics,* 2014, vol. 25, no. 6, p. 996–1003. DOI: 10.1109/JSEE.2014.00114

[16] XIONG, W., ZHANG, G., LIU, W. Efficient filter design against interrupted sampling repeater jamming for wideband radar. *EURASIP Journal on Advances in Signal Processing,* 2017, p. 1–12. DOI: 10.1186/s13634-017-0446-3

[17] YUAN, H., WANG, C., LI, X., et al. A method against interrupted-sampling repeater jamming based on energy function detection and band-pass filtering. *International Journal of Antennas and Propagation,* 2017, p. 1–9. DOI: 10.1155/2017/6759169

[18] CHEN, J., WU, W., XU, S., et al. Band pass filter design against interrupted-sampling repeater jamming based on time-frequency analysis. *IET Radar Sonar & Navigation,* 2019, vol. 13, no. 10, p. 1646–1654. DOI: 10.1049/iet-rsn.2018.5658

[19] ZHOU, C., LIU, Q., CHEN, X. Parameter estimation and suppression for DRFM-based interrupted sampling repeater jammer. *IET Radar Sonar & Navigation,* 2018, vol. 12, no. 1, p. 56 to 63. DOI: 10.1049/iet-rsn.2017.0114

[20] REN, Z., JIANG, M., ZHANG, L. Orthogonal phase-frequency coded signal in a pulse against interrupted sampling repeater jamming. *The Journal of Engineering,* 2019, no. 21, p. 7573–7576. DOI: 10.1049/joe.2019.0500

[21] ZHONG, S., HUANG, X., WANG, H., et al. Anti-intermittent sampling repeater jamming waveform design based on immune genetics. In *IEEE International Conference on Power, Intelligent*

Computing and Systems (ICPICS). Shenyang (China), 2019, p. 553 to 559. DOI: 10.1109/ICPICS47731.2019.8942420

[22] CAO, F., CHEN, Z., FENG, X., et al. Optimal design of anti-interrupted sampling repeater jamming waveform for missile-borne radar based on an improved genetic algorithm. *IET Signal Processing,* 2021, vol. 15, no. 9, p. 622–32. DOI: 10.1049/sil2.12066

[23] ZHOU, K., LI, D., SU, Y., et al. Joint design of transmit waveform and mismatch filter in the presence of interrupted sampling repeater jamming. *IEEE Signal Processing Letters,* 2020, vol. 27, p. 1610 to 1614. DOI: 10.1109/LSP.2020.3021667

[24] ZHOU, K., LI, D., QUAN, S., et al. SAR waveform and mismatched filter design for countering interrupted-sampling repeater jamming. *IEEE Transactions on Geoscience and Remote Sensing,* 2022, vol. 60, p. 1–14. DOI: 10.1109/TGRS.2021.3107328

[25] WANG, F., LI, N., PANG, C., et al. Complementary sequences and receiving filters design for suppressing interrupted sampling repeater jamming. *IEEE Geoscience and Remote Sensing Letters,* 2022, vol. 19, p. 1–5. DOI: 10.1109/LGRS.2022.3156164

[26] GE, M., YU, X., YAN, Z., et al. Joint cognitive optimization of transmit waveform and receive filter against deceptive interference. *Signal Processing,* 2021, vol. 185, p. 1–15. DOI: 10.1016/j.sigpro.2021.108084

[27] BEHRENS, R. T., SCHARF, L. L. Signal processing applications of oblique projection operators. *IEEE Transactions on Signal Processing,* 1994, vol. 42, no. 6, p. 1413–1424. DOI: 10.1109/78.286957

[28] BOYER, R. Oblique projection for source estimation in a competitive environment: Algorithm and statistical analysis. *Signal Processing,* 2009, vol. 89, no. 12, p. 2547–2554. DOI: 10.1016/j.sigpro.2009.04.023

[29] DING, M., WEI, Y., YU, L., et al. Adaptive suppression of mainlobe spread Doppler clutter with high directivity for HFSSWR using oblique projection. *Electronics Letters,* 2019, vol. 55, no. 23, p. 1245–1247. DOI: 10.1049/el.2019.1583

[30] DANG, H. Stepped frequency chirp signal SAR imaging. In *The 1st Asian and Pacific Conference on Synthetic Aperture Radar.* Huangshan (China), 2007, p. 14–18. DOI: 10.1109/APSAR.2007.4418544

[31] INALA, V., MANMADHARAO, G. Analysis of stepped frequency pulse train. In *International Conference on Radar, Communication and Computing (ICRCC).* Tiruvannamalai (India), 2012, p. 107 to 111. DOI: 10.1109/ICRCC.2012.6450557

[32] PRICE, R., HOFSTETTER, E. Bounds on the volume and height distributions of the ambiguity function. *IEEE Transactions on Information Theory,* 1965, vol. 11, no. 2, p. 207–214. DOI: 10.1109/TIT.1965.1053746

[33] SINSKY, A., WANG, C. Standardization of the definition of the radar ambiguity function. *IEEE Transactions on Aerospace and Electronic Systems,* 1974, vol. 10, no. 4, p. 532–533. DOI: 10.1109/TAES.1974.307831

[34] ZHANG, Y., WEI, Y., YU, L. Interrupted sampling repeater jamming recognition and suppression based on phase-coded signal processing. *Signal Processing,* 2022, vol. 198, p. 1–7. DOI: 10.1016/j.sigpro.2022.108596

[35] HE, H., STOICA, P., LI, J. On synthesizing cross ambiguity functions. In *IEEE International Conference on Acoustics, Speech and Signal Processing.* Prague (Czech Republic), 2011, p. 3536–3539. DOI: 10.1109/ICASSP.2011.5946241

[36] KUNDU, D. Modified MUSIC algorithm for estimating DOA of signals. *Signal Processing,* 1996, vol. 48, no. 1, p. 85–90. DOI: 10.1016/0165-1684(95)00126-3